Pneumatic Transport of Granular Materials with Electrostatic Effects

Eldin Wee Chuan Lim
Dept. of Chemical and Biomolecular Engineering, National University of Singapore, Singapore 117576, Singapore

Jun Yao
School of Energy Research, Xiamen University, Xiamen 361005, People's Republic of China

Institute of Particle Science and Engineering, School of Process, Environmental and Materials Engineering, University of Leeds, Leeds LS2 9JT, United Kingdom

Yanlin Zhao
Institute of Particle Science and Engineering, School of Process, Environmental and Materials Engineering, University of Leeds, Leeds LS2 9JT, United Kingdom

DOI 10.1002/aic.12638

The methodology of coupling large eddy simulation (LES) with the discrete element method was applied for computational studies of pneumatic transport of granular materials through vertical and horizontal pipes in the presence of electrostatic effects. The LES numerical results obtained agreed well with the law of the wall for various y^+*-ranges. The simulations showed that a thin layer of particles formed and remained adhered to the pipe walls during the pneumatic conveying process due to the effects of strong electrostatic forces of attraction toward the pipe walls. Particle concentrations were generally higher near the pipe walls than at the pipe center resulting in the ring flow pattern observed in previous experimental studies. The close correspondence between particle velocity vectors and fluid drag force vectors was indicative of the importance of fluid drag forces in influencing particle behaviors. In contrast, the much weaker particle–particle electrostatic repulsion forces had negligible effects on particle behaviors within the system under all operating conditions considered. The electrostatic field strength developed during pneumatic conveying increased with decreasing flow rate due to increased amount of particle-wall collisions. Based on dynamic analyses of forces acting on individual particles, it may be concluded that electrostatic effects played a dominant role in influencing particle behaviors during pneumatic conveying at low flow rates, whereas drag forces became more important at high flow rates.* © 2011 American Institute of Chemical Engineers *AIChE J,* 58: 1040–1059, 2012

Keywords: pneumatic transport, electrostatics, large eddy simulation, discrete element method, numerical simulation

Introduction

Triboelectrification is the process of charge acquisition by solid particulate materials during flows due to repeated collisions between the solid particles with surfaces of a different

---

Correspondence concerning this article should be addressed to J. Yao at yaojun@xmu.edu.cn.

material. It is an important phenomenon that arises in various environmental and industrial processes especially those that involve bounded turbulent flows of solid particulate materials. In recent years, the behaviors of granular materials under the effects of electrostatics have been investigated by several researchers. For example, the behaviors of small, conductive particles (<<1 mm) in known electric fields generated using a pair of parallel plates with alternating or direct voltages applied have been studied. The clustering patterns of such granular materials have been observed to be dependent on the voltage applied[1–3] as well as the humidity of the environment.[4] A similar phenomenon was observed by Yao et al.[5] for larger particles with diameter 2.8 mm where three characteristic aggregation patterns referred to as clusters, half-ring and ring were observed to form during pneumatic conveying through a vertical pipe in the presence of electrostatic effects. Al-Adel et al.[6] investigated the effect of static electrification on gas–solid flows in vertical risers and captured qualitative features of riser flows: core-annular particle distribution, annular particle downflow at low riser gas velocities, and annular upflow at high gas velocities. Joseph and Klinzing[7] demonstrated that choking of granular flow was caused by electrostatic effects in vertical pneumatic transport. On the other hand, electrostatic effects were dependent on a variety of factors such as the physical, chemical, and electrical characteristics of the material used and ambient conditions. Smeltzer et al.[8] performed tests in a pneumatic conveying system using glass beads and found that at constant loadings small particles exhibited greater electrostatic effects than large particles. Matsusaka et al.[9] developed a formulation for the variation of granule charging caused by repeated impacts on a wall and used the formulation to granule charging in granular flows where each granule carried a different amount of charge. They then analyzed theoretically the granule charge distribution. Recently, Yao and Wang[10] developed a method to investigate the effects of granule size and shape on electrostatics generation in pneumatic conveying systems and demonstrated that the proposed method is a useful tool for characterization of electrostatic effects in systems where granules have different sizes and geometries.

On the other hand, many researchers have considered the motions of ensembles of particles of various sizes and densities using numerical methods as reviewed by Crowe,[11] McLaughlin,[12] and Elghobashi.[13] The use of direct numerical simulation (DNS) techniques imposed severe restrictions on the ranges of parameters that could be studied because of the high computational demands. As such, DNS studies of particle motions in boundary layer flows had been confined to low Reynolds numbers and short simulation times. This had meant that only particles with short relaxation times in simple geometries could be studied.[14–17] In dilute systems, the effect of turbulence on particle motion had to be considered, whereas the converse was usually assumed to be negligible. With this assumption, the continuous phase could be treated separately from the particulate phase. However, when higher particle loadings were considered (volume fraction $> 10^{-6}$), particles significantly affected the turbulent flow field and two-way coupling between the phases had to be applied.[18] At even higher particle concentrations (volume fraction $> 10^{-3}$), particle–particle interactions also became important.[13] To model high Reynolds number flows within reasonable computational times, large eddy simulation (LES) has become a widely used technique in recent years. With LES, information regarding the small scales of turbulence is lost. In multiphase flows involving solid particulate materials, this is not a severe loss because it may be assumed that particles do not respond to these small scale turbulence effects due to the high density ratio between the particulate and the continuous phases.

In this study, the methodology of coupling LES with the discrete element method (DEM) was used to study pneumatic transport of granular materials through vertical pipes in the presence of electrostatic effects. Flows at three Reynolds numbers ($Re_D = 34 \times 10^3$, 38×10^3, 55×10^3) were considered. The particle size used was $d_p = 2.8$ mm, and the influence of electrostatic forces on particle behaviors was investigated. Particle concentrations and distributions near the pipe wall were found to depend on gas flow rates. A dynamical analysis examining the main forces acting on individual particles (gravity, buoyancy, and drag) was carried out to understand the mechanisms giving rise to the observed particle behaviors.

Mathematical Model

Continuous phase

LES Method. The incompressible form of the three-dimensional, unsteady Navier-Stokes equations is given by:

$$\nabla \cdot U = 0 \tag{1}$$

$$\frac{\partial U}{\partial t} + \nabla \cdot (UU) = -\nabla p + \frac{1}{Re_\tau}\nabla^2 U \tag{2}$$

where the quantities have been made dimensionless by u_τ and δ.

Top-hat filtering, implemented through finite-volume implicit grid-filtering, was used to generate the equations governing the transport of the large eddies. After filtering, the equations of motion became the following:

$$\nabla \cdot \bar{u} = 0 \tag{3}$$

$$\frac{\partial \bar{u}_i}{\partial t} + \frac{\partial}{\partial x_j}\left(\bar{u}_i\bar{u}_j\right) = -\frac{\partial \bar{P}}{\partial x_i} + \frac{\partial}{\partial x_j}\left[\left(\frac{1}{Re_\tau} + v_T\right)\frac{\partial \bar{u}_i}{\partial x_j}\right] + \frac{\partial}{\partial x_j}\left(v_T\frac{\partial \bar{u}_j}{\partial x_i}\right) + 4\delta_{i3} - f_d \tag{4}$$

The "over-bar" notation denotes application of the top-hat filter. The second last term on the right-hand side of (4) represents the mean streamwise pressure gradient that balances the total shear force for a fully developed pipe flow. The filtered pressure gradient $\partial\bar{P}/\partial x_i$ excludes the mean streamwise pressure gradient but includes the normal (or diagonal) components of the subgrid scale stresses. The eddy viscosity, v_T was determined from the subgrid kinetic energy, as described in the following section. The drag force f_d in dense gas–solid flow could be calculated by Eqs. 30–34 to be presented later.

Subgrid Modeling. The dynamic subgrid kinetic energy model used in this work, given in detail by Kim and

Menon,[19] can be summarized as follows. The transport equation for the subgrid kinetic energy, k_{sgs}, is given as:

$$\frac{\partial k_{\mathrm{sgs}}}{\partial t} + \overline{u}_i \frac{\partial k_{\mathrm{sgs}}}{\partial x_i} = \nu_{\mathrm{T}} \left| \overline{S} \right|^2 - \varepsilon + \frac{\partial}{\partial x_i}\left(\nu_{\mathrm{T}} \frac{\partial k_{\mathrm{sgs}}}{\partial x_i} \right) \tag{5}$$

where the eddy viscosity, ν_{T}, is given by

$$\nu_{\mathrm{T}} = C_{\mathrm{t}} \overline{\Delta} k_{\mathrm{sgs}}^{1/2} \tag{6}$$

and the dissipation rate, ε, is given by

$$\varepsilon = C_{\mathrm{e}} \frac{k_{\mathrm{sgs}}^{3/2}}{\overline{\Delta}} \tag{7}$$

where $\overline{\Delta}$ is the grid scale and C_{e} and C_{t} are dynamically determined. The resolved strain-rate tensor, $\overline{S}$ is expressed as

$$\overline{S}_{ij} = \frac{1}{2}\left(\frac{\partial \overline{u}_i}{\partial x_j} + \frac{\partial \overline{u}_j}{\partial x_i} \right) \tag{8}$$

and its magnitude is defined as

$$\left| \overline{S} \right| = \sqrt{2 \overline{S}_{ij} \overline{S}_{ij}} \tag{9}$$

Let the "hat" notation symbolize the application of the test filter to a quantity and the "overbar" notation symbolize application of the grid filter. The Leonard stress tensor is then defined as

$$L_{ij} = \widehat{\overline{u}_i \overline{u}_j} - \widehat{\overline{u}}_i \widehat{\overline{u}}_j \tag{10}$$

The kinetic energy at the test filter level can be found from the trace of

$$k_{\mathrm{test}} = \frac{1}{2}\left(\widehat{\overline{u}_k \overline{u}_k} - \widehat{\overline{u}}_k \widehat{\overline{u}}_k \right) \tag{11}$$

The dissipation at the test filter level is expressed as

$$\varepsilon_{\mathrm{test}} = (\nu + \nu_{\mathrm{T}}) \left(\widehat{\frac{\partial \overline{u}_i}{\partial x_j} \frac{\partial \overline{u}_i}{\partial x_j}} - \frac{\partial \widehat{\overline{u}}_i}{\partial x_j} \frac{\partial \widehat{\overline{u}}_i}{\partial x_j} \right) \tag{12}$$

Through a similarity assumption between the subgrid stress tensor and the Leonard stress tensor, one can arrive at the following equation:

$$L_{ij} = -2 C_{\mathrm{t}} \widehat{\Delta} k_{\mathrm{test}}^{1/2} \widehat{\overline{S}}_{ij} + \frac{1}{3} \delta_{ij} L_{kk} \tag{13}$$

The least-square method of Lilly[20] is then used to obtain a formula for C_{t}

$$C_{\mathrm{t}} = \frac{1}{2} \frac{L_{ij} \sigma_{ij}}{\sigma_{ij} \sigma_{ij}} \tag{14}$$

where

$$\sigma_{ij} = -\widehat{\Delta} k_{\mathrm{test}}^{1/2} \widehat{\overline{S}}_{ij} \tag{15}$$

By invoking a similarity assumption between the dissipation at the test filter and grid filter levels, an equation for the dissipation at the test filter level is given as

$$\varepsilon_{\mathrm{test}} = C_{\mathrm{e}} \frac{k_{\mathrm{test}}^{3/2}}{\widehat{\Delta}} \tag{16}$$

One may now calculate C_{t} and C_{e}. These constants have been constrained to be positive in the current simulations.

Cylindrical Co-Ordinate System. The momentum and continuity equations used in this study are in cylindrical coordinate system and given below.

$$\frac{\partial \overline{q_{\mathrm{z}}}}{\partial z} + \frac{\partial \overline{q_{\mathrm{r}}}}{\partial r} + \frac{\partial \overline{q_{\theta}}}{\partial \theta} = 0 \tag{17}$$

$$\begin{aligned} \frac{\partial \overline{q_{\theta}}}{\partial t} = {} & -\frac{1}{r}\frac{\partial \overline{p}}{\partial \theta} + \frac{1}{r}\frac{\partial}{\partial z}\left(\widehat{\tau}_{\theta \mathrm{z}} - \overline{q}_{\theta} \overline{q}_{\mathrm{z}} \right) \\ & + \frac{1}{r^2}\frac{\partial}{\partial r}\left(r^2 \widehat{\tau}_{\theta \mathrm{r}} - r \overline{q}_{\theta} \overline{q}_{\mathrm{r}} \right) + \frac{1}{r}\frac{\partial}{\partial \theta}\left(\widehat{\tau}_{\theta\theta} - \overline{q}_{\theta} \overline{q}_{\theta} \right) \end{aligned} \tag{18}$$

$$\begin{aligned} \frac{\partial \overline{q_{\mathrm{r}}}}{\partial t} = {} & -r \frac{\partial \overline{p}}{\partial r} + \frac{\partial}{\partial z}\left(\widehat{\tau}_{\mathrm{rz}} - \frac{\overline{q}_{\mathrm{r}} \overline{q}_{\mathrm{z}}}{r} \right) + \frac{\partial}{\partial r}\left(\widehat{\tau}_{\mathrm{rr}} - \frac{\overline{q}_{\mathrm{r}} \overline{q}_{\mathrm{r}}}{r} \right) \\ & + \frac{\partial}{\partial \theta}\left(\widehat{\tau}_{\mathrm{r}\theta} - \frac{\overline{q}_{\mathrm{r}} \overline{q}_{\theta}}{r} \right) - \left(\widehat{\tau}_{\theta\theta} - \overline{q}_{\theta} \overline{q}_{\theta} \right) \end{aligned} \tag{19}$$

$$\begin{aligned} \frac{\partial \overline{q_{\mathrm{z}}}}{\partial t} = {} & -r \frac{\partial \overline{p}}{\partial z} + \frac{\partial}{\partial z}\left(\widehat{\tau}_{\mathrm{zz}} - \frac{\overline{q}_{\mathrm{z}} \overline{q}_{\mathrm{z}}}{r} \right) \\ & + \frac{\partial}{\partial r}\left(\widehat{\tau}_{\mathrm{zr}} - \frac{\overline{q}_{\mathrm{z}} \overline{q}_{\mathrm{r}}}{r} \right) + \frac{1}{r}\frac{\partial}{\partial \theta}\left(\widehat{\tau}_{\mathrm{z}\theta} - \overline{q}_{\mathrm{z}} \overline{q}_{\theta} \right) \end{aligned} \tag{20}$$

where q_{z} represents axial flux $r \cdot v_{\mathrm{w}}$ (v_{w} is the axial velocity), q_{r} is radial flux $r \cdot v_{\mathrm{r}}$ (v_{r} is the radial velocity) and $q_{\theta} = v_{\theta}$.

The stress is given as follows:

$$\widehat{\tau}_{ij} = (1 + \nu_{\mathrm{T}} Re) \overline{S_{ij}} \tag{21}$$

where the eddy viscosity ν_{T} is shown in Eq. 6 according to the subgrid model used and the strain tensor expressed by the variables q_i is:

$$\begin{pmatrix} S_{\mathrm{zz}} & S_{\mathrm{zr}} & S_{\mathrm{z}\theta} \\ S_{\mathrm{zr}} & S_{\mathrm{rr}} & S_{\mathrm{r}\theta} \\ S_{\mathrm{z}\theta} & S_{\mathrm{r}\theta} & S_{\theta\theta} \end{pmatrix} = \begin{pmatrix} \frac{\partial q_{\mathrm{z}}}{\partial z} & \frac{1}{2}\left[\frac{\partial q_{\mathrm{z}}}{\partial r} + \frac{\partial q_{\mathrm{r}}}{\partial z} - \frac{q_{\mathrm{z}}}{r} \right] & \frac{1}{2}\left[\frac{\partial q_{\mathrm{z}}}{\partial \theta} + r \frac{\partial q_{\theta}}{\partial z} \right] \\ S_{\mathrm{zr}} & \left[\frac{\partial q_{\mathrm{r}}}{\partial r} - \frac{q_{\mathrm{r}}}{r} \right] & \frac{1}{2}\left[\frac{\partial q_{\theta}}{\partial r} + \frac{1}{r^2}\frac{\partial q_{\mathrm{r}}}{\partial \theta} - \frac{q_{\theta}}{r} \right] \\ S_{\mathrm{z}\theta} & S_{\mathrm{r}\theta} & \left[\frac{1}{r}\frac{\partial q_{\theta}}{\partial \theta} + \frac{q_{\mathrm{r}}}{r^2} \right] \end{pmatrix} \tag{22}$$

Numerical Procedures. The governing equations were, in accordance with the symmetry of the geometry, expressed in cylindrical coordinates as shown in the previous section. The equations were solved using a second-order finite volume method with central differencing of spatial derivatives on a staggered grid. Diffusion terms were handled with the Crank-Nicholson scheme and convective terms with the second-order Adams-Bashforth scheme. The Harlow-Welch fractional step method was used to solve the pressure Poisson equation resulting from the fractional step method. Uniform computational grid was applied to the circumferential and axial directions. In the radial direction, nonuniform meshes specified by a hyperbolic tangent function were used.

Periodic boundary condition was applied in the axial direction as the simulated pipe flow was fully developed. On the pipe wall, the usual no-slip boundary condition was applied. Because of the cylindrical co-ordinate system used in this work, a singularity existed at the centerline of the pipe ($r = 0$), which made it difficult to specify boundary conditions for all velocity components at the pipe center. Unger and Friedrich[21] argued that no boundary conditions are needed as the grid surface area goes to zero, and therefore, the momentum and mass fluxes are also zero. In this work, another approach was taken to deal with this by solving the fluxes (r times velocity components) instead of the velocity variables directly as shown in Eqs. 17–20. Therefore, at the centerline, a value of zero was specified for all three variables used in the equations.

Most of the computations for a pipe of length $L_z = 10R$ were performed using a $65 \times 39 \times 65$ grid but the influence of the grid resolution on the accuracy of the solution was investigated. The finest grid ($129 \times 49 \times 129$) led to well resolved simulations. The $65 \times 39 \times 65$ grid captured all of the features of the flow although small differences between some of the statistics obtained with these two grids were discernable. As the finer grid required much longer CPU time and greater storage requirements, simulations were performed using the $65 \times 39 \times 65$ grid which gave a good compromise between CPU time and accuracy. The final statistics were obtained by spatial averaging in the homogeneous streamwise and circumferential directions and time-averaging. The simulation results will be validated in the following sections.

The computational grid constructed was nonuniform in the radial direction with more nodes near the wall boundary. With a pipe radius of 0.5, the $i_{\max}$ nodes were distributed according to a hyperbolic tangent function:

$$r_i = 0.5 \times \tan h\left(\frac{i}{2i_{\max}} \ln\left(\frac{1+c}{1-c}\right)\right) \tag{23}$$

where c is an adjustable constant. To have the first grid point located at $y^+ \approx 1.5$ and the second at $y^+ \approx 5$, we took for c the value of 0.22 in cases with $Re_\mathrm{b} = 56.2 \times 10^3$, $c = 0.30$ for $Re_\mathrm{b} = 38.6 \times 10^3$, and $c = 0.34$ for $Re_\mathrm{b} = 33.4 \times 10^3$. Here, Re_b is defined as the Reynolds number based on the bulk velocity and pipe diameter. The Re_τ based on the friction velocity u_τ and pipe diameter can be obtained once the friction velocity is known. Based on Blasius' law,[22] the friction velocities could be calculated to be 0.0133 m s^{-1} for $Re_\mathrm{b} = 56.2 \times 10^3$, 0.0096 m s^{-1} for $Re_\mathrm{b} = 38.6 \times 10^3$ and 0.0085 m s^{-1} for $Re_\mathrm{b} = 33.4 \times 10^3$ yielding friction Reynolds numbers of 534, 383, and 337, respectively. It should be mentioned here that LES at a higher Reynolds number but with the same number of grid points would give less accurate results, especially with respect to the smaller scales.

Discrete element method

The methodology of DEM and its corresponding governing equations have been presented numerous times in the research literature[23–27] and only a brief description will be presented here for sake of completeness. The method of implementation followed that used by Lim et al.[28,29] in their numerical studies of pneumatic conveying of granular materials through vertical, horizontal, and inclined pipes. The translational and rotational motions of individual solid particles are governed by Newton's laws of motion:

$$m_i \frac{dv_i}{dt} = \sum_{j=1}^{N} \left(f_{\mathrm{c},ij} + f_{\mathrm{d},ij}\right) + m_i g + f_{\mathrm{f},i} + f_{\mathrm{e},i} \tag{24}$$

$$I_i \frac{d\omega_i}{dt} = \sum_{j=1}^{N} T_{ij} \tag{25}$$

where m_i and v_i are the mass and velocity of ith particle, respectively, N is the number of particles in contact with ith particle, $f_{\mathrm{c},ij}$ and $f_{\mathrm{d},ij}$ are the contact and viscous contact damping forces, respectively, $f_{\mathrm{f},i}$ is the fluid drag due to the interstitial fluid, $f_{\mathrm{e},i}$ is the electrostatic force, I_i is the moment of inertia of ith particle, ω_i is its angular velocity, and T_{ij} is the torque arising from contact forces which causes the particle to rotate.

Contact and damping forces have to be calculated using force-displacement models that relate such forces to the relative positions, velocities, and angular velocities of the colliding particles. Following previous studies,[23–29] a linear spring-and-dashpot model was implemented for the calculation of these collision forces. With such a closure, interparticle collisions are modeled as compressions of a perfectly elastic spring, whereas the inelasticities associated with such collisions are modeled by the damping of energy in the dashpot component of the model. Collisions between particles and a wall may be handled in a similar manner but with the latter not incurring any change in its momentum. In other words, a wall at the point of contact with a particle may be treated as another particle but with an infinite amount of inertia. The normal ($f_{\mathrm{cn},ij}$, $f_{\mathrm{dn},ij}$) and tangential ($f_{\mathrm{ct},ij}$, $f_{\mathrm{dt},ij}$) components of the contact and damping forces are calculated according to the following equations:

$$f_{\mathrm{cn},ij} = -\left(\kappa_{\mathrm{n},i}\delta_{\mathrm{n},ij}\right)n_i \tag{26}$$

$$f_{\mathrm{ct},ij} = -\left(\kappa_{\mathrm{t},i}\delta_{\mathrm{t},ij}\right)t_i \tag{27}$$

$$f_{\mathrm{dn},ij} = -\eta_{\mathrm{n},i}(v_\mathrm{r} \cdot n_i)n_i \tag{28}$$

$$f_{\mathrm{dt},ij} = -\eta_{\mathrm{t},i}\left\{(v_\mathrm{r} \cdot t_i)t_i + \left(\omega_i \times R_i - \omega_j \times R_j\right)\right\} \tag{29}$$

where $\kappa_{\mathrm{n},i}$, $\delta_{\mathrm{n},ij}$, n_i, $\eta_{\mathrm{n},i}$ and $\kappa_{\mathrm{t},i}$, $\delta_{\mathrm{t},ij}$, t_i, $\eta_{\mathrm{t},i}$ are the spring constants, displacements between particles, unit vectors, and viscous contact damping coefficients in the normal and tangential directions, respectively, v_r is the relative velocity between particles, and R_i and R_j are the radii of particles i and j, respectively. If $|f_{\mathrm{ct},ij} > |f_{\mathrm{cn},ij}| \tan\varphi$, then "slippage" between two contacting surfaces is simulated based on Coulomb-type friction law, i.e., $|f_{\mathrm{ct},ij}| = |f_{\mathrm{cn},ij}| \tan\varphi$, where $\tan\phi$ is analogous to the coefficient of friction.

The fluid drag force model proposed by Di Felice[30] which is applicable over a wide range of particle Reynolds numbers was used to evaluate the drag force. The equations in this fluid drag force model include:

$$f_{\mathrm{f},i} = f_{\mathrm{f0},i}\varepsilon_i^{-(\chi+1)} \tag{30}$$

$$f_{\mathrm{f0},i} = 0.5c_{\mathrm{d0},i}\rho_\mathrm{f}\pi R_i^2\varepsilon_i^2|u_i - v_i|(u_i - v_i) \tag{31}$$

$$\chi = 3.7 - 0.65\exp\left[-\frac{\left(1.5 - \log_{10} Re_{\mathrm{p},i}\right)^2}{2}\right] \tag{32}$$

$$c_{\mathrm{d0},i} = \left(0.63 + \frac{4.8}{Re_{\mathrm{p},i}^{0.5}}\right)^2 \tag{33}$$

$$Re_{\mathrm{p},i} = \frac{2\rho_\mathrm{f}R_i\varepsilon_i|u_i - v_i|}{\mu_\mathrm{f}} \tag{34}$$

where $f_{\mathrm{f0},i}$ is the fluid drag force on particle i in the absence of other particles, χ is an empirical parameter, ε_i is the local average porosity in the vicinity of particle i, $c_{\mathrm{d0},i}$ is the drag coefficient, $Re_{\mathrm{p},i}$ is the Reynolds number based on particle diameter, ρ_f is the fluid density, μ_f is the fluid viscosity, and u_i is the fluid velocity.

Under the two-way coupling approach for modeling fluid-particle interactions, the calculation of f_d requires numerical interpolation of gas-phase velocity, pressure, and void fraction from neighboring nodes to particle locations. In this work, this has been handled by an interpolation method that is in fact a convex combination of information at neighboring nodes in the 3-D case. By Newton's law, the total particle-to-gas force in a cell can be calculated by integrating the drag forces acting on all particles inside the cell. Because of the utilization of a staggered grid for velocity and pressure discretization, the particle-to-gas force may once more be interpolated to the location of velocity nodes.

Electrostatics effect

During pneumatic conveying, solid particles gain electrostatic charges as a result of repeated collisions and impacts against other particles and with the walls of the conveying pipe. The amount of charge transferred between two contacting bodies during impact depends on the potential difference between the two bodies, which in turn depends on their surface work functions and the image charge effect. In addition, the large group of charged particles within a conveying line gives rise to an electric field that can also influence the total potential difference through what is known as the space charge effect. It may be expected that a comprehensive mathematical model which incorporates such effects would be necessary for a detailed transient simulation of the electrification of particles starting from uncharged ones. Such a model is beyond the scope of this study. Instead, it was assumed that the pneumatic conveying system had been operated beyond the transient state of electrification such as to reach a dynamic state of electrostatic equilibrium.[18] The amount of charge carried by the particles as well as the walls of the pipe then remained fairly constant with respect to time. In general, charges are transferred between particles and the pipe walls during particle-wall collisions due to differences in material properties between the two contacting bodies while charge transfer between two colliding particles may occur due to differences in electrical potential or charge densities. At the state of electrostatic equilibrium, it may be expected that particles and the pipe walls are oppositely charged relatively to each other as all particles carry the same type of charges. In other words, attractive electrostatic forces exist between particles and pipe walls while repulsive electrostatic forces exist between any pair of particles. The total electrostatic force acting on each particle may then be written as the sum of electrostatic forces due to charges carried by other particles and the pipe walls.

$$f_{\mathrm{e},i} = f_{\mathrm{ep},i} + f_{\mathrm{ew},i} \tag{35}$$

where $f_{\mathrm{ep},i}$ and $f_{\mathrm{ew},i}$ are the electrostatic forces due to other charged particles and the pipe walls acting on particle i, respectively. It may also be mentioned at this point that at the state of electrostatic equilibrium, the linear charge density of the pipe walls is assumed to give rise to electrostatic forces of attraction acting on particles near the walls that are much more significant than image charge forces. In other words, it is assumed that image charge forces are negligible in comparison with the electrostatic forces due to charged pipe walls when the state of electrostatic equilibrium has been attained.

The electrostatic force arising from charges carried by other particles may be calculated by assuming each particle to be a constant point charge.

$$f_{\mathrm{ep},i} = \sum_{\substack{j=1 \\ j\neq i}}^{N} \frac{Q^2}{4\pi\varepsilon_\mathrm{o}r_{ij}^2}n_i \tag{36}$$

where Q is the constant charge assumed to be carried by all particles, ε_o is the permittivity of free space, r_{ij} is the distance between particles i and j, and n_i is the unit normal vector in the direction of the line joining the two particle centers.

The average electric field strength near a wall of the pneumatic conveying pipe may be estimated by assuming the pipe to be a flat plat infinitely long in the axial direction.[29]

$$E = \int \frac{1}{4\pi\varepsilon_0}\cdot\frac{dq}{r^2} = \frac{\lambda}{2\pi\varepsilon_0 d}\int_0^{\frac{\pi}{2}} \cos\theta d\theta = \frac{\lambda}{2\pi\varepsilon_0 d} \tag{37}$$

where E is the electric field strength, q is the equilibrium charge on the pipe wall, ε_o is the permittivity of free space, r is the average distance of particles to the pipe wall, and λ is the linear charge density along the pipe wall. The electrostatic force on a charged particle i located near the pipe wall may then be calculated as $f_{\mathrm{ew},i} = E{\cdot}Q$.

The geometry of the pneumatic conveying system and type of particles used in this simulations are summarized in Tables 1 and 2. These were based on the experimental work of Yao et al.[31] so that a meaningful comparison between the simulation and experimental outputs can be made. The overall solid fraction was about 5% as applied in the experimental studies of the previous researchers. In all simulations performed, particles were first allowed to settle freely under gravity for 0.5 s before gas flow was initiated. Periodic boundary conditions were applied to the solid phase to simulate an open flow system. Particles which were carried out of the conveying pipe by the flowing gas were simulated to re-enter from the inlet of the pipe with the same velocities and radial positions.

Table 1. Material Properties and System Parameters

Shape of Particles	Spherical
Particle diameter, d	2.8 mm
Particle density, ρ_p	1123 kg m^{-3}
Coefficient of restitution	0.9
Coefficient of friction	0.3
Gas density, ρ_f	1.205 kg m^{-3}
Gas viscosity, μ_f	1.8×10^{-5} N s m^{-2}
Pipe diameter	0.04 m
Pipe length	1.0 m
Computational cell size	4 mm × 4 mm
Simulation time step, Δt	10^{-6} to 10^{-5} s

The particle response time can be calculated as follows:

$$\tau_p = \frac{\rho_p d_p^2}{18\rho_{\mathrm{flow}} v} = 32.39\,\mathrm{s} \tag{38}$$

The dimensionless time step used for integration of the governing equations in LES was 1.0×10^{-4}. Based on the following equation:

$$t = \frac{t^+ v}{\mu_\tau^2} \tag{39}$$

it may be seen that for the three flow velocities considered in this work with corresponding values of μ_τ equal to 0.008, 0.009, 0.013 m s^{-1}, the dimensional time steps required are 2.36×10^{-5}, 1.86×10^{-5}, and 8.93×10^{-6} s, respectively. It is thus clear that the integral time scale of turbulence is much smaller than the particle response time and hence sufficient to resolve the particle trajectories.

Results and Discussion

Flow field simulation

Mean Velocity. It is known that in wall-bounded turbulent flows, such as pipe flows, channel flows, and boundary layers, several flow regimes each having their own flow characteristics and scaling parameters will be present. Normally, a distinction is made between a so-called inner and an outer layer. The inner layer consists of the near-wall region, in which the flow is assumed to be independent of the large scale geometry. In other words, the flow quantities in the inner layer are similar regardless of whether the flow geometry takes the form of a pipe, channel, or flat plate. The outer layer on the other hand depends on the geometry of the flow. Of course, a region of overlap between the two layers exists in which a gradual transition from one layer into the other occurs.

Table 2. Electrostatic Parameters for Vertical Pneumatic Conveying Simulations

Inlet Gas Velocity (m s^{-1})	Particle Charge Density (10^{-9} C g^{-1})	Pipe Wall Linear Charge Density λ (C m^{-1})
12.6	2.36	-1.57×10^{-5}
14.6	2.05	-3.27×10^{-6}
21.2	1.22	-1.14×10^{-6}

Figure 1 shows the mean velocity profiles, nondimensionalized with the friction velocity u_τ, along the entire pipe cross section. These data were plotted in the usual semi-logarithmic manner using inner scaling. For comparison, the universal curves defined by $W^+ + = y^+$ ($y^+ < 5$) and $W^+ = A \ln y^+ + B(y^+ > 30)$ were plotted. The mean velocity profile in a turbulent pipe flow at high Reynolds numbers may be described as follows. Very near the wall, in the viscous sublayer where $y^+ < 5$, the Reynolds stress was negligible and w^+ grew linearly with y^+, $W^+ = y^+$. Conversely, in the limit of an infinite Reynolds number, the turbulent inertial region where $y^+ > 30$ was characterized by a negligible viscous stress and a dominant Reynolds stress. Modeling the Reynolds stress in this region by the linear mixing-length approach of Prandtl[32] resulted in the "logarithmic velocity distribution law" $W^+ = A \ln y^+ + B$. For fully developed pipe flows at high Reynolds numbers, the experimental data indicated that $A = 2.5$ and $B = 5.0$. However, for low Reynolds numbers the additive constant B took a value of 5.5.[33] These equations specified the law of the wall for various y^+-ranges. The values of the constants A and B are still a matter of dispute, as there is considerable scatter in these values as determined from experiments. In Figure 1, all three measured profiles tended toward $W^+ = y^+$ as the layer $0 < y^+ < 5$ was approached.

Figure 1 also shows that the characteristics of the profiles compared quite well, although the simulated profiles were slightly higher than the universal curve, as was found in several experiments. The higher Reynolds number LES curve showed some discrepancies with the other curves in the so-called buffer layer. This deviation could be attributed to the limited resolution of the simulation and the performance of the SGS modeling in this buffer layer. Presumably, a more

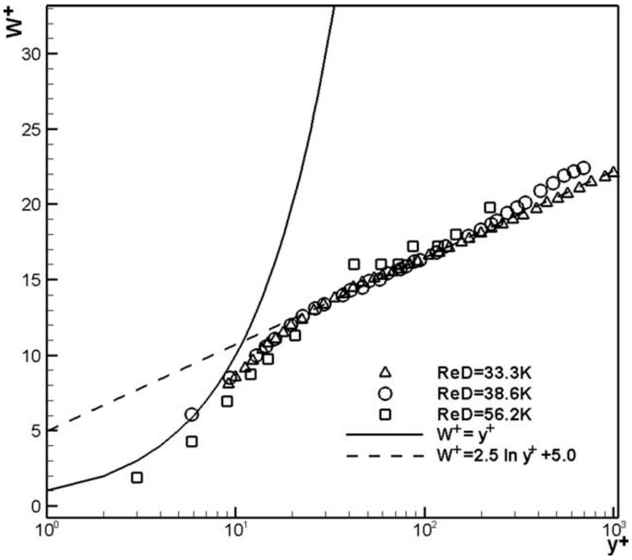

Figure 1. Measured mean velocity profile scaled on inner variables for three different Reynolds numbers: 33.3×10^3, 38.6×10^3, and 56.2×10^3 (corresponding to flow rates 950, 1100, and 1600 L min^{-1}).

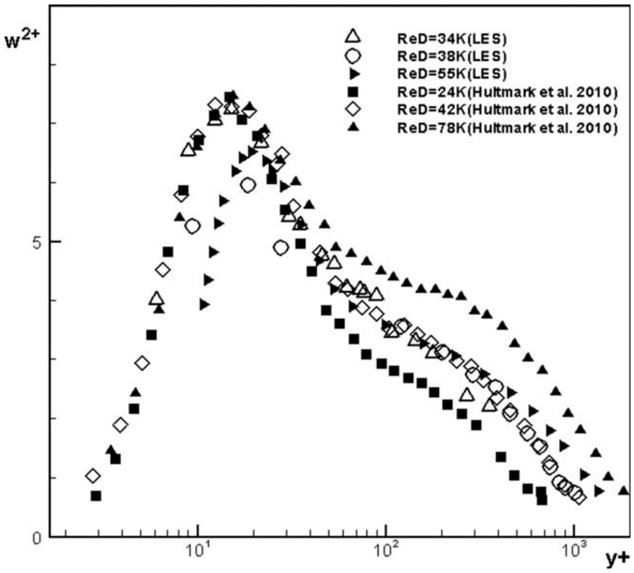

Figure 2. Streamwise turbulence intensity distributions for pipe flow plotted in inner coordinates.

advanced dynamic SGS model reflecting the local properties of turbulence would be more appropriate in this case.

Turbulence Intensity. Figure 2 shows turbulence intensities for the streamwise direction. The inhomogeneity and anisotropy of the turbulence properties could be observed. It is seen that the maximum value of the axial turbulence intensity was located at around a fixed position irrespective of Reynolds number, in agreement with the work of Mochizuki and Nieuwstadt[34] which concluded from a survey of data taken in boundary layer, pipe, and channel flows that this peak was independent of Reynolds number, and therefore followed classical scaling. Classical scaling worked very well for the mean velocity profile, as comprehensively demonstrated by Zagarola and Smits[35] and McKeon et al.[36] Figure 2 shows that the streamwise turbulence intensity profiles obtained in this work and other previous studies exhibited a peak in w^{+2} near $y^+ = 15$ which was independent of Reynolds number, and therefore followed classical scaling.

Electrostatic field

The electrostatic field strength in a pneumatic conveying system is determined by the amount of charges accumulated on the pipe walls at the state of electrostatic equilibrium. As the state of electrostatic equilibrium is established, it is possible to evaluate the time-invariant electrostatic field strength.[31] The electrostatic field strength due to the charged pipe walls of the vertical pipe was calculated according to Eq. 37 for the three flow rates considered in this study. It was assumed that charges were evenly distributed along the pipe walls. Figure 3 shows that for all cases, the highest electrostatic field strength appeared near the pipe walls and degraded toward the pipe center. In addition, the electrostatic field strength at equilibrium increased with decreasing air flow rate. To evaluate the effects of the electrostatic field on particle behaviors without complications from other dynamic factors such as fluid drag and interparticle collisions, the

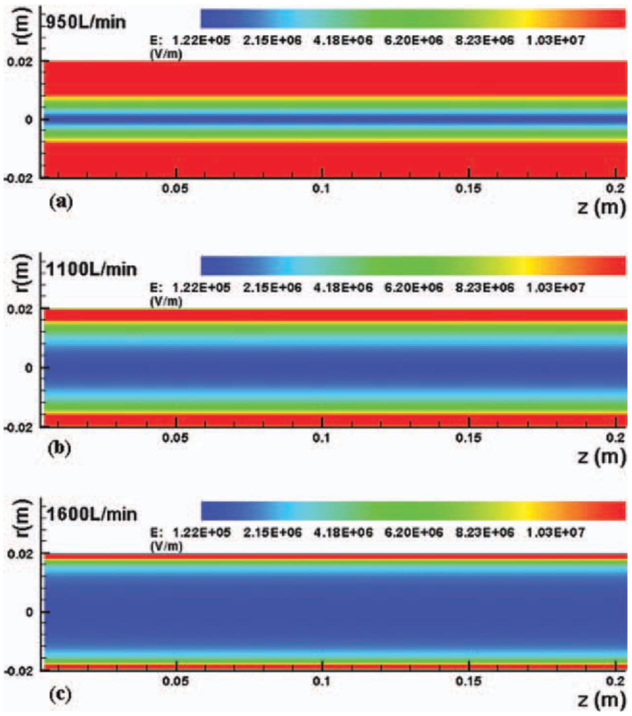

Figure 3. Electrostatic field strength distribution of charged pipe wall in *r–z* plane for three flows ($E = 1.22 \times 10^5 \sim 1.22 \times 10^7$ V m^{-1}, 150 contour levels were applied and scaled linearly between the minimum and maximum levels): (a) 950, (b) 1100, (c) 1600 L min^{-1}.

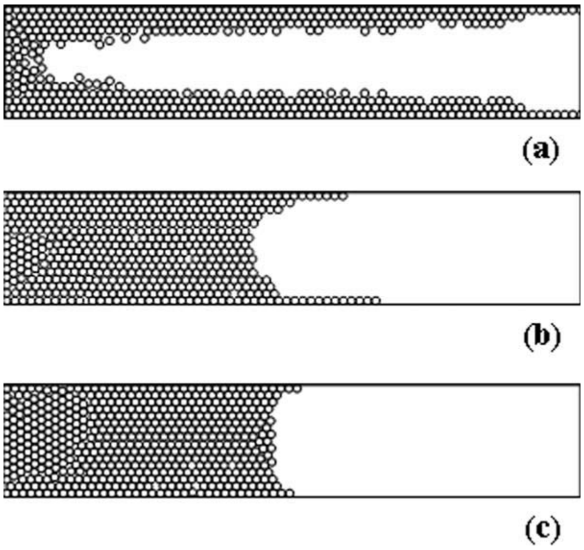

Figure 4. Particle distributions after settling under gravity in the presence of electrostatic effects but without air flow.

The electrostatic field strengths applied corresponded to those that will be developed under the state of electrostatic equilibrium at air flow rates of (a) 950, (b) 1100, and (c) 1600 L min^{-1}. The direction of gravity is toward the left of each panel. Only the bottom 0.2 m section of each vertical pneumatic conveying pipe is shown.

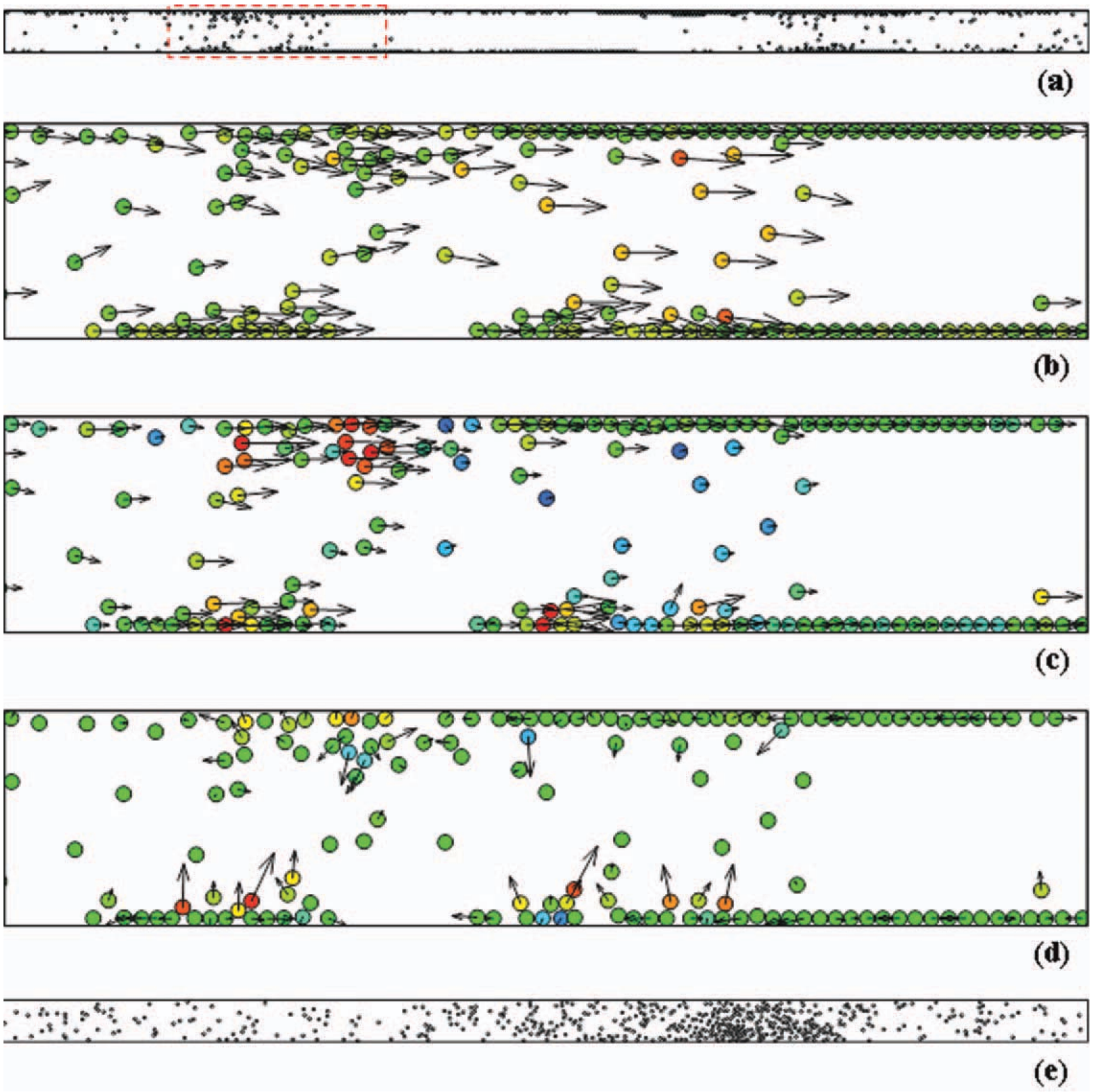

Figure 5. (a) Instantaneous particle distribution during vertical pneumatic conveying at an air flow rate of 950 L min^{-1} in the presence of electrostatic effects.

The region marked by a dashed box is enlarged in the next three panels. (b) Instantaneous particle velocity vectors with color contours indicating magnitudes of axial components of particle velocities ranging linearly from 0 m s^{-1} (blue) to 12.6 m s^{-1} (red). (c) Instantaneous fluid drag force vectors with color contours indicating magnitudes of axial components of fluid drag forces ranging linearly from 0 N (blue) to 2.0×10^{-4} N (red). (d) Instantaneous interparticle electrostatic repulsion force vectors with color contours indicating radial components of interparticle electrostatic repulsion forces ranging linearly from -10^{-6} N (blue) to 10^{-6} N (red). (e) Instantaneous particle distribution during vertical pneumatic conveying at an air flow rate of 950 L min^{-1} in the absence of electrostatic effects. The direction of gravity is toward the left of each panel.

distributions of particles after settling under gravity for 0.5 s in the presence of electrostatic effects but without air flow were analyzed. Figure 4a shows that a thin layer of particles adhered stably to the pipe walls under the effects of an electrostatic field corresponding to that which would be developed under the state of electrostatic equilibrium at an air flow rate of 950 L min^{-1}. At higher air flow rates where the strengths of the electrostatic fields developed were lower, the tendencies for particles to be adhered to the pipe walls were also correspondingly lower. It would be seen later that these would have implications for solid concentration profiles developed over the cross sections of the pipe during the actual pneumatic conveying process.

Figure 5a shows an instantaneous snapshot of the pneumatic conveying process obtained from DEM simulations for an air flow rate of 950 L min^{-1}. The state of electrostatic equilibrium was assumed to be established throughout the conveying process. As with the previous simulation involving particles settling under gravity, it may also be seen here that a thin layer of particles remained adhered to the pipe walls under the effects of strong electrostatic forces of attraction toward the pipe walls. Particle concentrations were generally higher near the pipe walls than at the pipe center and such a flow pattern would correspond to the ring flow pattern observed in previous experimental studies.[5] Figure 5b shows that most particles in the conveying pipe moved in

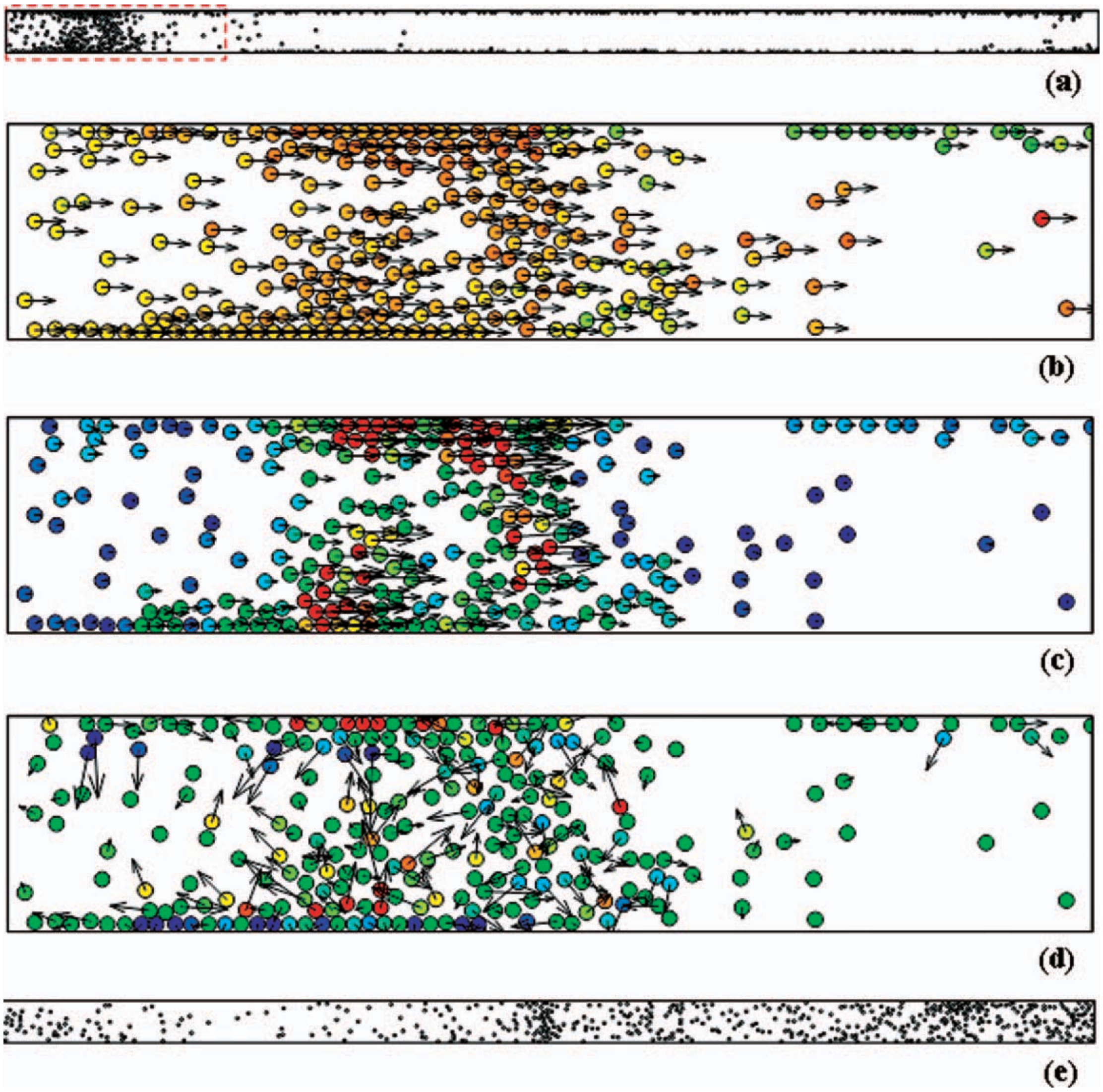

Figure 6. (a) Instantaneous particle distribution during vertical pneumatic conveying at an air flow rate of 1100 L min^{-1} in the presence of electrostatic effects.

The region marked by a dashed box is enlarged in the next three panels. (b) Instantaneous particle velocity vectors with color contours indicating magnitudes of axial components of particle velocities ranging linearly from 0 m s^{-1} (blue) to 14.6 m s^{-1} (red). (c) Instantaneous fluid drag force vectors with color contours indicating magnitudes of axial components of fluid drag forces ranging linearly from 0 N (blue) to 5.0×10^{-4} N (red). (d) Instantaneous interparticle electrostatic repulsion force vectors with color contours indicating radial components of interparticle electrostatic repulsion forces ranging linearly from -10^{-6} N (blue) to 10^{-6} N (red). (e) Instantaneous particle distribution during vertical pneumatic conveying at an air flow rate of 1100 L min^{-1} in the absence of electrostatic effects. The direction of gravity is toward the left of each panel.

the axial direction. Particle velocities were generally higher near the pipe center than at the pipe walls due to similar air velocity profiles developed over the cross section of the pipe. However, it may also be seen that most particles moved at much lower velocities than the average gas velocity of 12.6 m s^{-1}. Figure 5c shows that fluid drag forces acting on particles were predominantly oriented in the axial direction, indicating that the direction of motion of particles was largely a result of fluid drag forces. Although electrostatic forces that arose due to particle–particle repulsion might have the effect of disrupting the almost unidirectional motion of particles, Figure 5d shows that such forces were much smaller in magnitudes than fluid drag forces and so did not exert significant effects on particle behaviors during the pneumatic conveying process. It may thus be concluded at this point that the ring flow pattern observed in experimental studies of pneumatic conveying through vertical pipes arose due to two predominant types of forces present within the system. Electrostatic forces of attraction resulted in the adherence of particles onto the pipe walls as fluid drag forces moved the particles along the pipe in the axial direction. These two aspects of solid pattern formation and solid motion had minimal disruptive effects on each other as the two types of forces that gave rise to them were oriented more or less normal to each other. In contrast, Figure 5e shows that particles were distributed fairly homogeneously in the radial direction during pneumatic conveying in the absence of any electrostatic effects. This is reminiscent of the

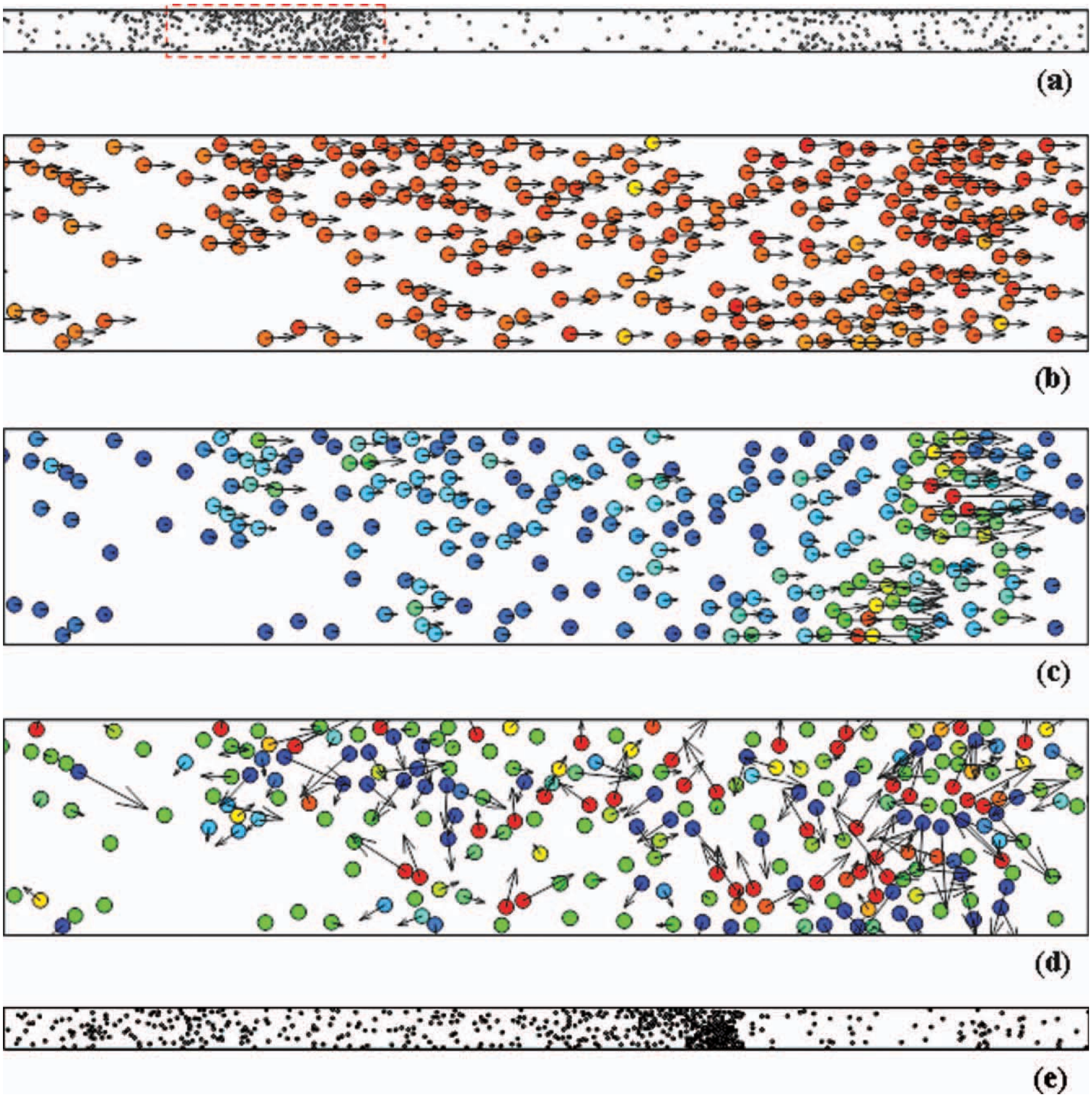

Figure 7. (a) Instantaneous particle distribution during vertical pneumatic conveying at an air flow rate of 1600 L min^{-1} in the presence of electrostatic effects.

The region marked by a dashed box is enlarged in the next three panels. (b) Instantaneous particle velocity vectors with color contours indicating magnitudes of axial components of particle velocities ranging linearly from 0 m s^{-1} (blue) to 21.2 m s^{-1} (red). (c) Instantaneous fluid drag force vectors with color contours indicating magnitudes of axial components of fluid drag forces ranging linearly from 0 N (blue) to 5.0×10^{-4} N (red). (d) Instantaneous interparticle electrostatic repulsion force vectors with color contours indicating radial components of interparticle electrostatic repulsion forces ranging linearly from -10^{-7} N (blue) to 10^{-7} N (red). (e) Instantaneous particle distribution during vertical pneumatic conveying at an air flow rate of 1600 L min^{-1} in the absence of electrostatic effects. The direction of gravity is toward the left of each panel.

dispersed flow pattern that had been observed in previous experimental studies where at the start of each pneumatic conveying experiment, the dispersed flow pattern was formed as the amount of electrostatic charges present on the particles as well as the pipe walls was negligible.[5]

Figure 6a shows that the flow pattern observed at a higher air flow rate of 1100 L min^{-1} was similar to that seen previously. Because of the slightly weaker electrostatic field present, a thinner layer of particles was seen adhered to most parts of the pipe walls. In addition, there was a tendency for particles to move in the form of clusters near the pipe center. Figure 6b shows that the predominant direction of particle motion was along the axis of the pipe. The close correspondence between the particle velocity vectors and fluid drag

Table 3. Dynamic Analysis for Individual Particles in Near Wall Region ($<r_p$)

Air Flow Rate (L min^{-1})	F_{Dr} (N)	F_{Dz} (N)	F_{Er} (N)	F_{fz} (N)
1600	3.45×10^{-4}	7.94×10^{-3}	5.16×10^{-7}	2.89×10^{-7}
1100	3.90×10^{-5}	6.70×10^{-4}	2.47×10^{-6}	1.38×10^{-6}
950	3.14×10^{-5}	5.60×10^{-4}	1.37×10^{-5}	7.68×10^{-6}

Particle weight: 1.26×10^{-4} N.

force vectors as seen in Figure 6c was again indicative of the importance of fluid drag forces in influencing particle behaviors. In comparison with the previous case, particles conveyed at a higher air flow rate were observed to move at velocities closer to the average gas velocity. Figure 6d shows that particle–particle electrostatic repulsion forces were typically oriented in more or less random directions and so were expected to cause deviation of particle velocities from the axial direction. Such forces acting on particles adhered to the pipe walls might also dislodge such particles from the pipe walls leading to destruction of the characteristic ring flow pattern. However, as with the previous case presented, Figure 6d shows that such particle–particle electrostatic repulsion forces were much smaller in magnitudes than both fluid drag forces and electrostatic forces of attraction exerted by the pipe walls and so their disruptive effects were not manifested in the flow patterns observed. Figure 6e shows that no layer of particles was seen adhered to the pipe walls in the absence of electrostatic effects thus further verifying that the contrasting phenomenon observed in the previous panels was a consequence of the electrostatic forces present.

At the highest air flow rate of 1600 L min^{-1} considered in this study, the flow pattern obtained from the DEM simulations shows that the characteristic ring flow pattern was no longer easily discernable due to much fewer particles remaining adhered to the pipe walls during the conveying process (Figure 7a). This was a direct consequence of the weak electrostatic field present under such flow conditions as seen in Figure 3 earlier. Figure 7b shows that most particles moved at velocities close to the average gas velocity and predominantly in the axial direction. As with the previous case, particle velocities were strongly influenced by fluid drag forces (Figure 7c) and the much weaker particle–particle electrostatic repulsion forces (Figure 7d) had negligible effect on particle behaviors within the system. Because of the weaker electrostatic field strength, the flow pattern developed was similar to that developed in the complete absence of electrostatic effects (Figure 7e). However, it would be seen in a later section via a more quantitative analysis of particle distribution within the conveying pipe that small differences in flow patterns could still be detected at this operating condition.

Dynamic analysis

The forces acting on individual particles near the wall boundary ($<r_p$) were calculated and the results summarized in Table 3. Drag forces in both the radial and axial directions (F_{Dr}, F_{Dz}) increased with air flow rate. For all cases considered, the drag force in the axial direction (F_{Dz}) was larger than the gravitational force acting on each particle so that particles could be transported upward in the vertical pipe. At an air flow rate of 1600 L min^{-1}, the drag force in the radial direction (F_{Dr}) was much larger than the electrostatic force acting on individual particles and this had the effect of causing particles to move away from the pipe walls

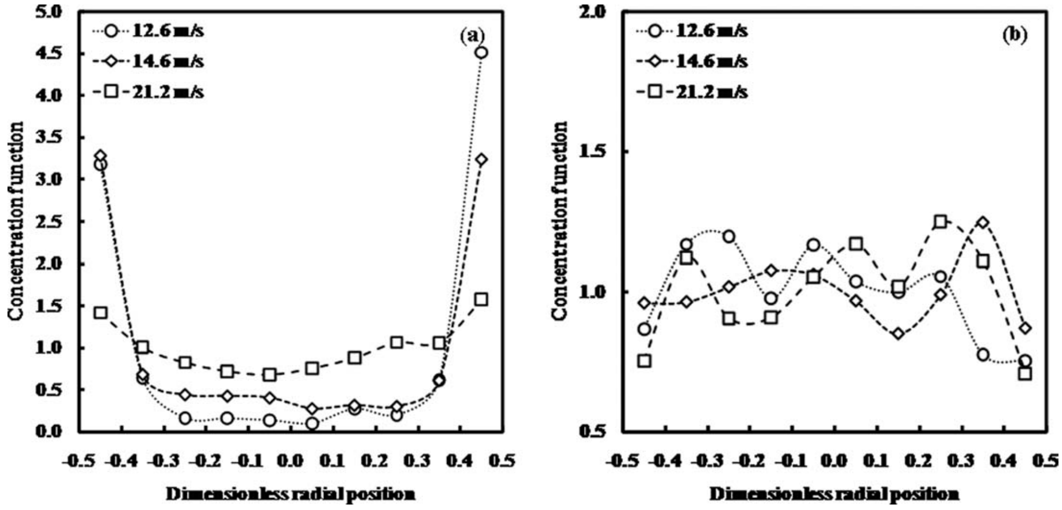

Figure 8. Concentration function profiles during vertical pneumatic conveying at various average gas velocities in the (a) presence and (b) absence of electrostatic effects.

Radial positions have been nondimensionalized by diameter of pipe.

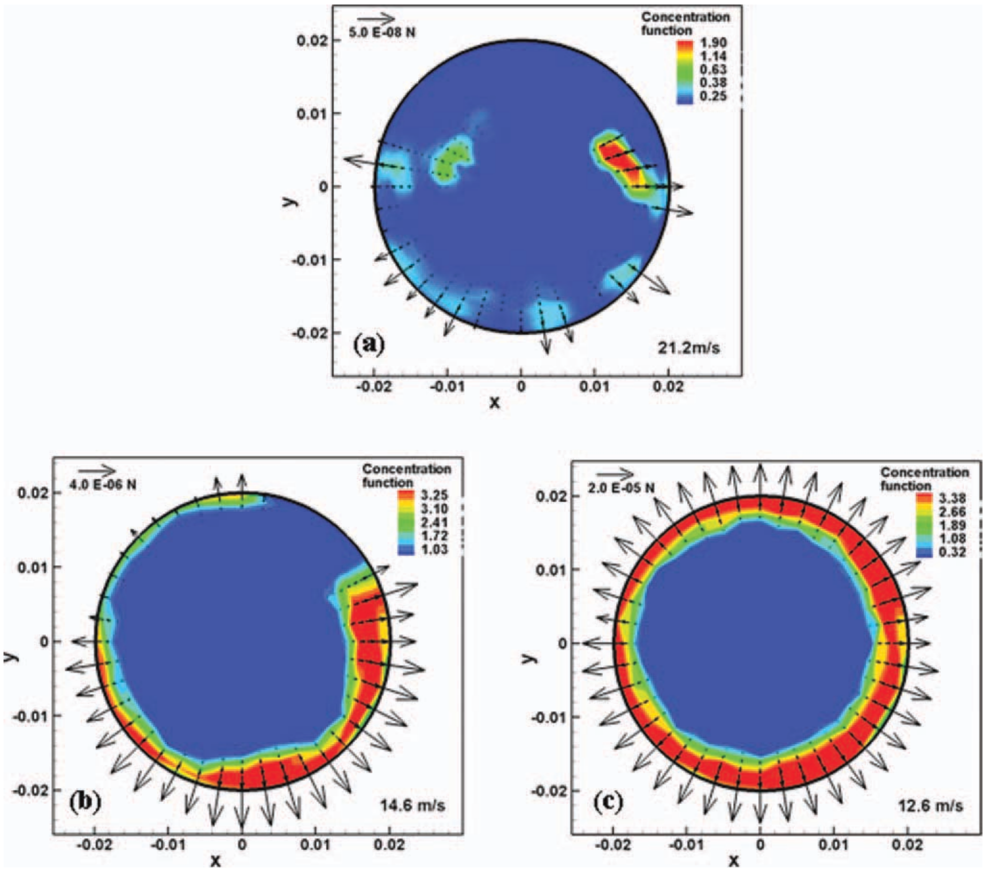

Figure 9. Electrostatic forces acting on granules and particle concentration distributions within the vertical pipe for the three flow rates: (a) 1600, (b) 1100, and (c) 950 L min^{-1}.

against the direction of electrostatic forces. As air flow rate was decreased, electrostatic forces in the radial direction increased. At an air flow rate of 950 L min^{-1}, the magnitude of electrostatic forces became similar to that of drag forces in the radial direction. Therefore, there was a tendency for particles to stick onto the pipe walls and form clusters in the shapes of a ring along the vertical pipe as observed in the experimental work of Yao et al.[5] previously.

The frictional force in the axial direction (F_{fz}) arising from particles adhering to the pipe walls due to electrostatic forces increased with increasing electrostatic forces (see Table 3). When compared with the drag force in the axial direction F_{Dz}, F_{fz} was lower but the difference in magnitudes between the two types of forces decreased with increasing air flow rate. In other words, the frictional force (F_{fz}) might play a more important role in affecting particle behaviors in the near wall region at lower air flow rates. It may also be noted that the frictional force defined here was based on the electrostatic force F_{Er} only and excluded the contribution from the drag force F_{Dr}. If a particle stuck onto the pipe wall, the drag force in the radial direction would be expected to contribute toward the frictional force (F_{fz}) to cause the particle to stay adhered on the pipe wall. For example, at the air flow rate of 950 L min^{-1}, $F_{\mathrm{Dr}} = 3.14 \times 10^{-5}$ N, whereas the corresponding $F_{\mathrm{fz}} = F_{\mathrm{Dr}} \times f = 3.14 \times 10^{-5} \times 0.56 = 1.76 \times 10^{-5}$ N. Based on the above dynamic analyses, it may be concluded that electrostatic effects played a more dominant role in influencing particle behaviors during pneumatic conveying through vertical pipes at low flow rates while drag forces became more important at high flow rates. This is in agreement with what may be inferred from spatially averaged profiles of particle concentration obtained from the DEM simulations. Following an analogous approach applied by Matida et al.[37] for analyzing particle concentration distribution, the pipe cross section was divided into 10 equal sampling strips and a dimensionless particle concentration function was obtained as follows:

$$\frac{\overline{C_i}}{\overline{C}} = \frac{N_{\mathrm{p}i}/\overline{u}_{\mathrm{p}i}}{\sum_i N_{\mathrm{p}i}/\overline{u}_{\mathrm{p}i}}\frac{A}{A_i} \qquad (40)$$

where $N_{\mathrm{p}i}$ is the number of particles sampled in strip i, $\overline{u}_{\mathrm{p}i}$ is the mean particle axial velocity, and A_i and A are the cross-sectional areas of the strip and entire pipe, respectively. Figure 8a shows profiles of the concentration function, $\frac{\overline{C_i}}{\overline{C}}$, obtained during pneumatic conveying at various air flow rates in the presence of electrostatic effects. The concentration function profile developed at the lowest air flow rate applied exhibited the largest difference in magnitudes between the near wall regions and at the pipe center corresponding to the ring flow

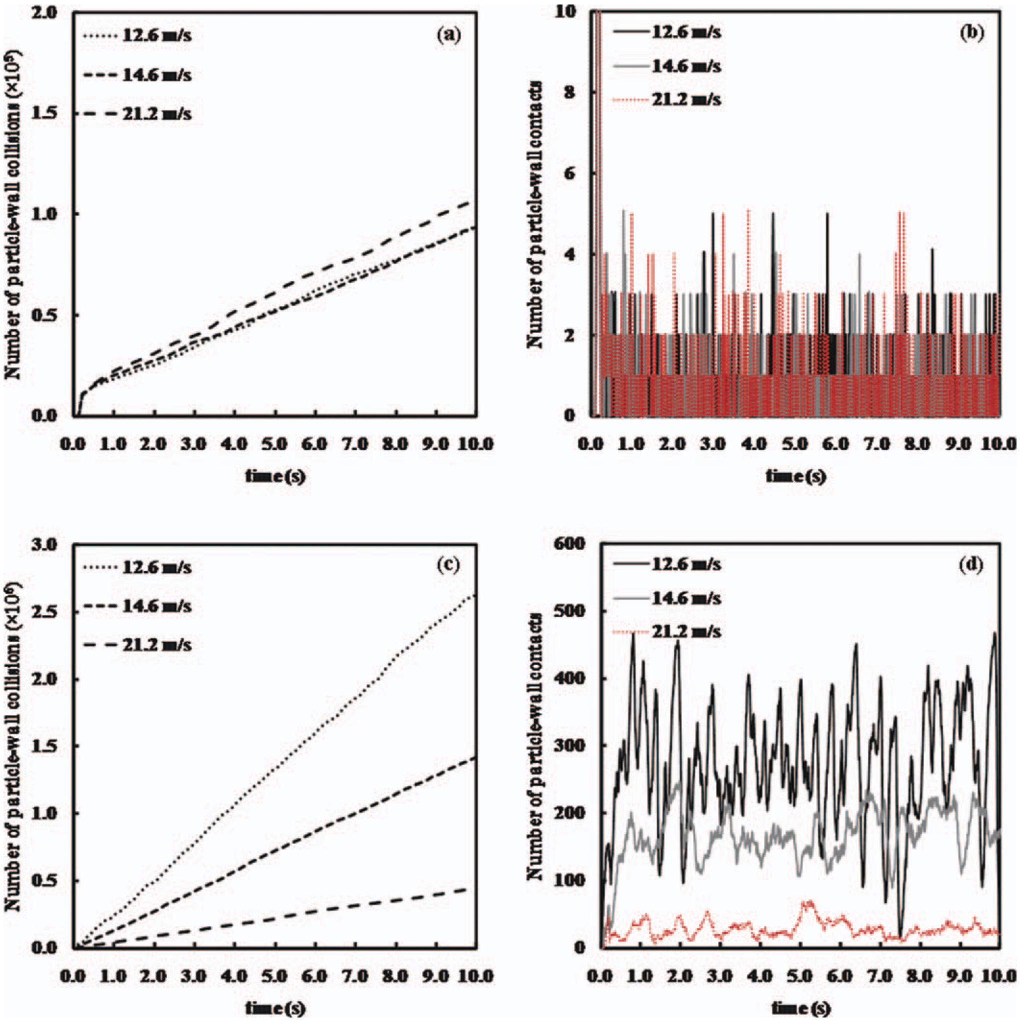

Figure 10. (a) Cumulative number of particle-wall collisions and (b) instantaneous number of particles in contact with pipe walls during vertical pneumatic conveying at various average gas velocities in the absence of electrostatic effects.

(c) Cumulative number of particle-wall collisions and (d) instantaneous number of particles in contact with pipe walls during vertical pneumatic conveying at various average gas velocities in the presence of electrostatic effects.

pattern. Such differences in the concentration function values diminished with increasing air flow rate indicating a corresponding drop in importance of electrostatic effects in influencing particle behaviors. In contrast, Figure 8b shows that the concentration function profiles obtained during pneumatic conveying in the absence of electrostatic effects fluctuated around a mean value of about 1.0 over the pipe cross section for all air flow rates considered. This implies that particles were more homogeneously distributed over the cross section of the pipe. The tendency for particles to reside near the pipe walls leading to the formation of the ring flow pattern that is characteristic of pneumatic conveying in the presence of electrostatic effects was absent in this case.

Figure 9 shows the particle concentration function over the cross section of the pipe together with vectors of electrostatic forces acting on the particles. It may be observed that the electrostatic field strength was fairly high near the pipe wall and diminished toward the pipe center. This was due to the fact that electrostatic charges were generated and resided on the pipe wall. With decreasing air flow rates, the electrostatic field strength increased and this was accompanied by an increase in surface charge density of granules as seen earlier in Table 2. This relationship between air flow rates and strength of electrostatic field developed during pneumatic conveying may be explained by the number of particle-wall collisions that occurred during the transport process. Figure 10a shows the cumulative number of particle-wall collisions during pneumatic conveying at various air flow rates in the absence of electrostatic effects. The cumulative number of collisions increased fairly linearly with time and there was minimal difference between the three flow rates considered. Figure 10b shows the instantaneous number of particles that were in contact with the pipe walls during the conveying process at various air flow rates. It may be observed that in the absence of electrostatic effects, the number of particles that remained in contact with the pipe walls was low for all

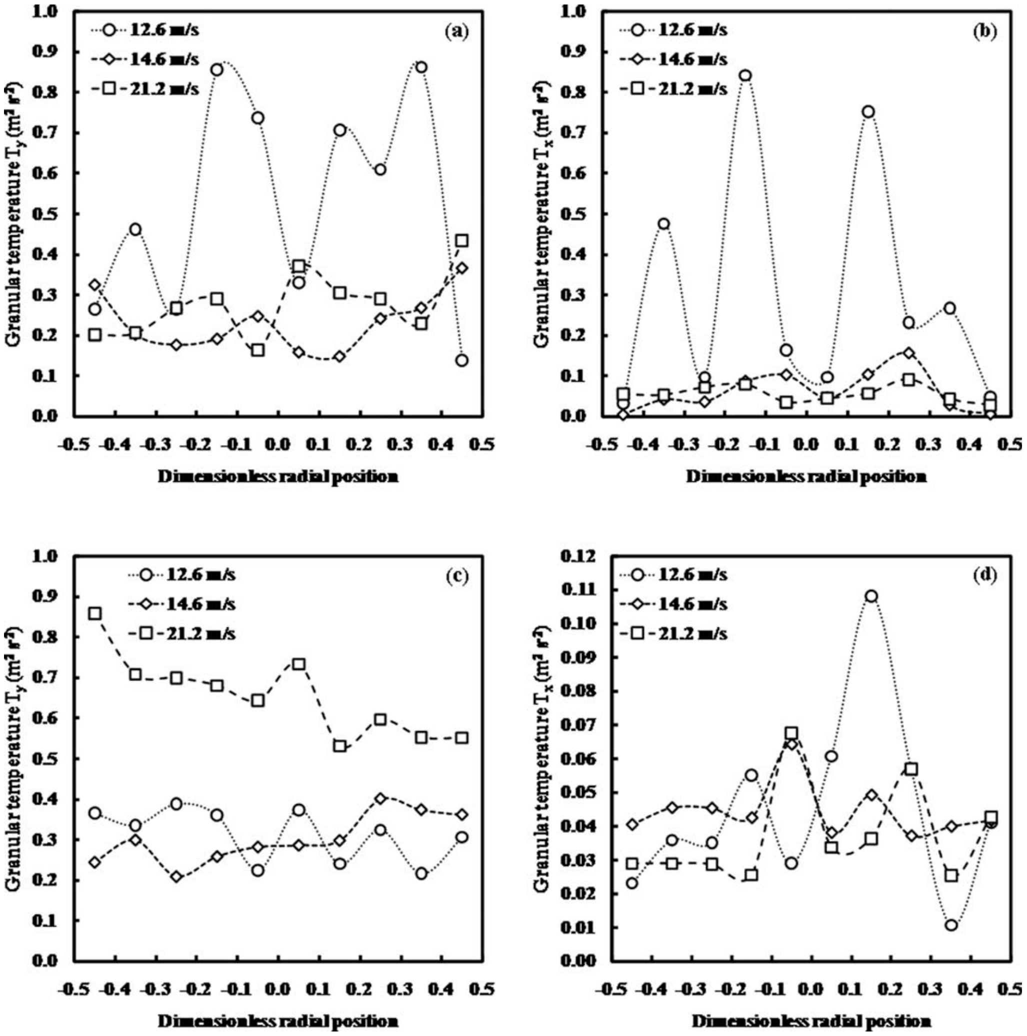

Figure 11. Spatially averaged granular temperature profiles: (a) T_y and (b) T_x for vertical pneumatic conveying in the presence of electrostatic effects as well as (c) T_y and (d) T_x for vertical pneumatic conveying in the absence of electrostatic effects.

Radial positions have been nondimensionalized by diameter of pipe.

flow rates considered. This was due to the dominance of the fluid drag force in determining the trajectories of particles within the pipe as discussed previously. In contrast, at the state of electrostatic equilibrium, Figure 10c shows that the cumulative number of particle-wall collisions increased much more rapidly during pneumatic conveying at lower flow rates than at higher flow rates. In comparisons with Figure 10a, the cumulative number of collisions was also seen to increase much more rapidly with time in the presence of electrostatic effects. Figure 10d also shows that the number of particles in contact with the pipe walls at any one instant in time was also higher during pneumatic conveying at lower flow rates than at higher flow rates. The number of instantaneous particle-wall contacts in the presence of electrostatic effects was also about two orders of magnitude larger compared with those seen in Figure 10b where electrostatic effects were absent. This is consistent with the development of stronger electrostatic field strengths during pneumatic conveying at lower flow rates than at higher flow rates observed in previous experimental studies.[5,31] Although the transient process of electrostatic charge generation and accumulation on particles and pipe walls had not been considered in the present study, it may be deduced based on the two cases presented here (one where electrostatic effect was absent and one where the state of electrostatic equilibrium had been established) that the rate of electrostatic charging is expected to be higher at lower flow rates as a result of larger number of particle-wall collisions and number of particles that remained in contact with the pipe walls during the pneumatic conveying process. This is a self-sustaining process in that stronger electrostatic forces, which are a consequence of larger number of particle-wall collisions, will be able to maintain the latter at a sufficiently high level that is necessary for the sustenance of the electrostatic field itself. Any flow patterns of the particles that arise as a result of the electrostatic field, such as the ring flow pattern, can thus be considered a fully developed feature of the pneumatic conveying process.

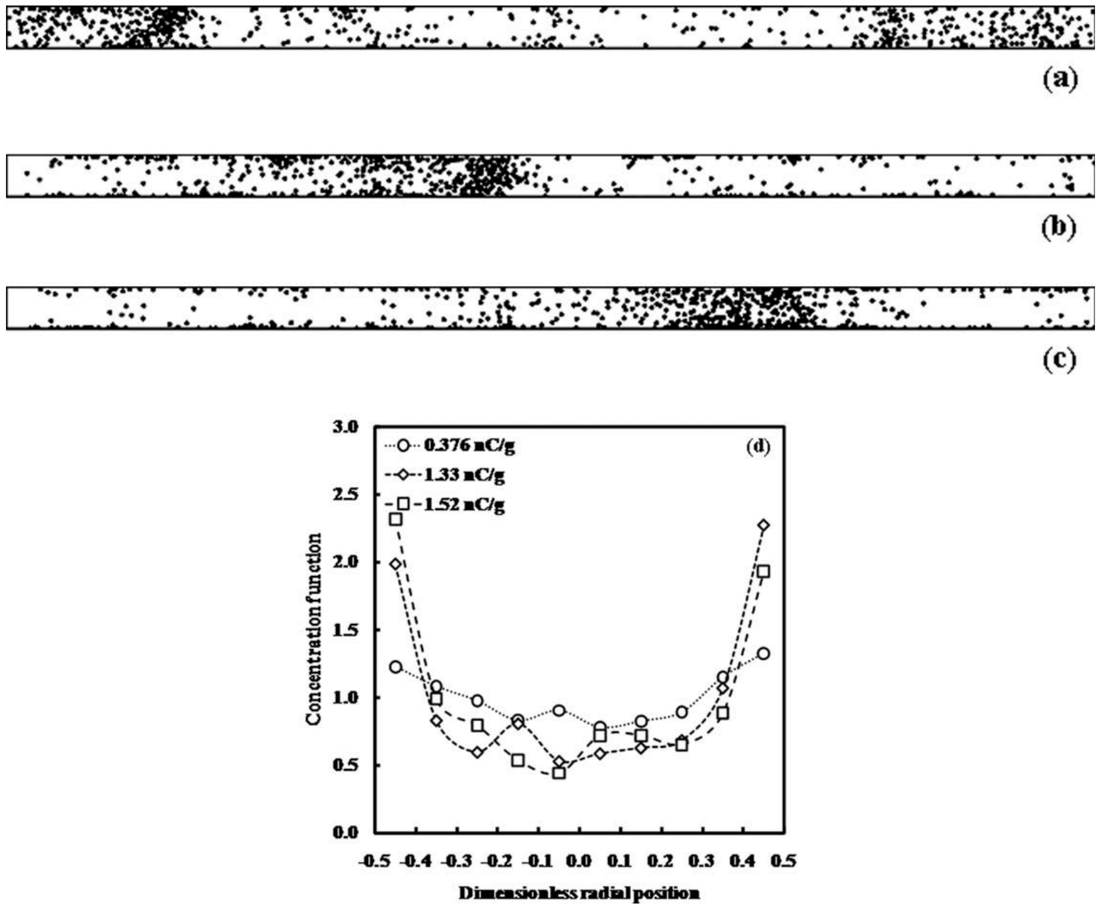

Figure 12. Instantaneous particle distribution during vertical pneumatic conveying at an air flow rate of 1600 L min^{-1} in the presence of electrostatic effects.

The particle charge densities are (a) 0.376 × 10^{-9} C g^{-1}, (b) 1.33 × 10^{-9} C g^{-1}, and (c) 1.52 × 10^{-9} C g^{-1}. (d) Concentration function profiles during vertical pneumatic conveying in the presence of electrostatic effects with the above particle charge densities.

Figures 11a, b show that granular temperatures were fairly isotropic during vertical pneumatic conveying in the presence of electrostatic effects. Here, $T_y = \frac{1}{2n}\sum_{i=1}^{n}\left(v_{y,i} - \overline{v_y}\right)^2$ and $T_x = \frac{1}{2n}\sum_{i=1}^{n}\left(v_{x,i} - \overline{v_x}\right)^2$, where $v_{y,i}$ and $v_{x,i}$ are the vertical and horizontal components of velocity of the *i*th particle, respectively, $\overline{v_y}$ and $\overline{v_x}$ are the corresponding mean velocities. Granular temperatures were highest at the lowest air flow rate considered, and this was likely due to the strongest electrostatic effects present. The magnitudes of granular temperatures at the other air flow rates of 1100 L min^{-1} and 1600 L min^{-1} were fairly similar. In contrast, Figures 11c, d show that granular temperatures were very anisotropic in the absence of electrostatic effects. The axial components of granular temperatures were about one order of magnitude higher than the corresponding radial components. Interestingly and in stark contrast to the previous case, the axial component of granular temperature was highest for the highest air flow rate applied in the absence of electrostatic effects. This implied that fluctuations in particle velocities were caused predominantly by electrostatic forces when electrostatic effects were present and by the flow of air otherwise.

The basis of all simulation results presented so far in this study was the attainment of the state of electrostatic equilibrium in the pneumatic conveying system. During the transient stage of electrostatic charge accumulation via tribocharging, solid flow patterns are expected to evolve gradually through time from one corresponding to absence of any electrostatic effects to that of electrostatic equilibrium. However, to our knowledge, studies of such solid flow pattern evolution in pneumatic conveying systems have not been reported in the literature to date. Yao et al.[5] reported experimental data of particle charge densities during the electrostatic charging process in a pneumatic conveying system. Particle charge densities were observed to increase with time

Table 4. Electrostatic Parameters for Horizontal Pneumatic Conveying Simulations

Inlet Gas Velocity (m s^{-1})	Particle Charge Density (10^{-9} C g^{-1})	Pipe Wall Linear Charge Density λ (C m^{-1})
12.6	2.36	-1.62×10^{-6}
14.6	2.05	-8.89×10^{-7}
21.2	1.22	-1.32×10^{-7}

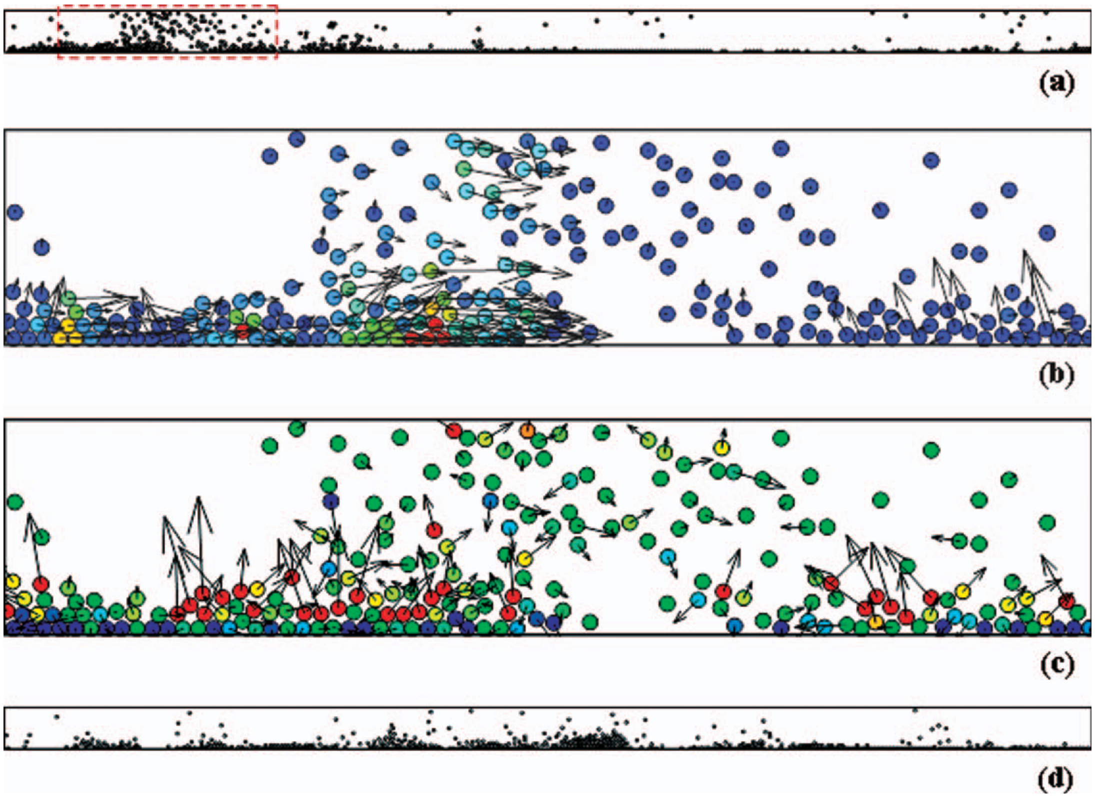

Figure 13. (a) Instantaneous particle distribution during horizontal pneumatic conveying at an air flow rate of 950 L min^{-1} in the presence of electrostatic effects.

The region marked by a dashed box is enlarged in the next three panels. (b) Instantaneous fluid drag force vectors with color contours indicating magnitudes of axial components of fluid drag forces ranging linearly from 0 N (blue) to 1.0×10^{-4} N (red). (c) Instantaneous interparticle electrostatic repulsion force vectors with color contours indicating radial components of interparticle electrostatic repulsion forces ranging linearly from -10^{-6} N (blue) to 10^{-6} N (red). (d) Instantaneous particle distribution during horizontal pneumatic conveying at an air flow rate of 950 L min^{-1} in the absence of electrostatic effects. The direction of gravity is downward.

during the first 3 h of operation. The values measured 66 min, 141 min, and 157 min after commencing operation of the pneumatic conveying system were 0.376×10^{-9} C g^{-1}, 1.33×10^{-9} C g^{-1}, and 1.52×10^{-9} C g^{-1}, respectively. These were used in this study to carry out simulations of the pneumatic conveying process during the transient stage of electrostatic charging and to construct the corresponding particle concentration function profiles. Figures 12a–c show that a gradual buildup of a layer of particles on the pipe walls occurred with the increase in particle charge densities. The solid flow pattern was indeed observed to evolve gradually from that of dispersed flow towards that of ring flow. This phenomenon is also seen more quantitatively in the particle concentration function profiles in Figure 12d. With a particle charge density of 0.376×10^{-9} C g^{-1} corresponding to the state of the pneumatic conveying system a short while after commencing operation, the concentration function profile was fairly uniform and similar to that presented earlier for a system without electrostatic effects. The concentration function became less uniform over the cross section of the conveying pipe with increasing particle charge density indicating that solid particles were accumulating on the pipe walls. Eventually, the concentration function profile approached that seen earlier for the system that had attained the state of electrostatic equilibrium.

With the completion of the above studies of pneumatic conveying through vertical pipes with electrostatic effects, it was deemed prudent to apply the computational methodology toward studies of horizontal pneumatic conveying. The electrostatic parameters applied here were also based on the experimental work of Yao et al.[31] and are shown in Table 4. On comparison with Table 2, it may be observed that particle charge densities developed during horizontal pneumatic conveying were approximately one order of magnitude smaller than those for vertical pneumatic conveying at corresponding air flow rates. As such, electrostatic effects were expected to play a less significant role in affecting solid flow patterns in the present case. Figure 13a shows an instantaneous snapshot of the horizontal pneumatic conveying process for an air flow rate of 950 L min^{-1}. It may be seen that particles in this case were asymmetrically distributed about the axis of the pipe due to the effect of gravitational settling. Fluid drag forces were oriented predominantly in the axial direction (Figure 13b), whereas particle–particle electrostatic repulsion forces were oriented randomly (Figure 13c). As in the case of vertical pneumatic conveying, the latter was much smaller in magnitude and so did not lead to dispersion of the particles. Figure 13d shows an instantaneous snapshot of the moving dunes flow pattern typically observed in horizontal pneumatic conveying at low solid concentrations in

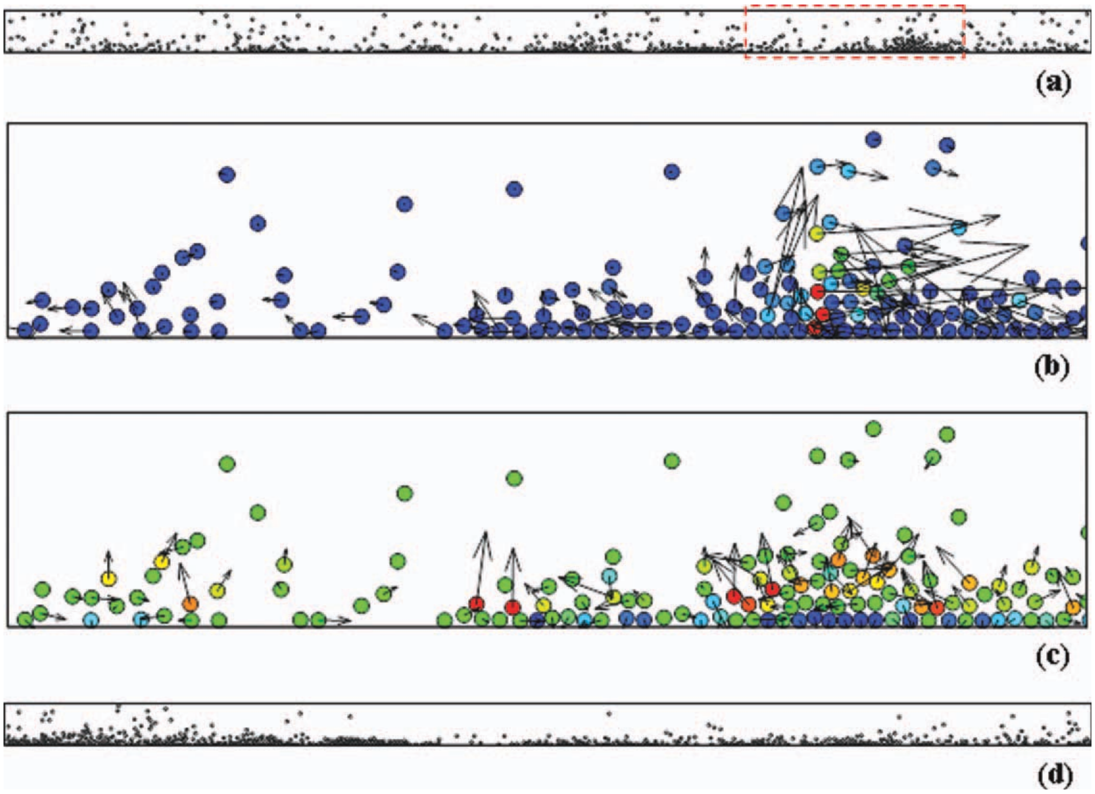

Figure 14. (a) Instantaneous particle distribution during horizontal pneumatic conveying at an air flow rate of 1100 L min^{-1} in the presence of electrostatic effects.

The region marked by a dashed box is enlarged in the next three panels. (b) Instantaneous fluid drag force vectors with color contours indicating magnitudes of axial components of fluid drag forces ranging linearly from 0 N (blue) to 1.0×10^{-4} N (red). (c) Instantaneous interparticle electrostatic repulsion force vectors with color contours indicating radial components of interparticle electrostatic repulsion forces ranging linearly from -10^{-6} N (blue) to 10^{-6} N (red). (d) Instantaneous particle distribution during horizontal pneumatic conveying at an air flow rate of 1100 L min^{-1} in the absence of electrostatic effects. The direction of gravity is downward.

the absence of electrostatic effects. Because of the much weaker electrostatic forces present during horizontal pneumatic conveying, the solid flow patterns developed at the state of electrostatic equilibrium were similar to those observed in the absence of any electrostatic effects. The above observations were also applicable to horizontal pneumatic conveying at air flow rates of 1100 L min^{-1} (Figure 14) and 1600 L min^{-1} (Figure 15), where electrostatic effects were even weaker. As such and for the sake of brevity, the above discussion would not be repeated for the latter two cases. Figures 16a, b show the concentration function profiles developed in the presence and absence of electrostatic effects respectively. There were only minimal differences between the profiles at different air flow rates in both cases thus supporting the earlier qualitative observations that electrostatic effects were less significant in affecting particle distributions within the pipe during horizontal pneumatic conveying.

Figures 17a, b show that granular temperatures were slightly anisotropic during horizontal pneumatic conveying in the presence of electrostatic effects with the axial component generally larger than the corresponding radial component. As in the case of vertical pneumatic conveying in the presence of electrostatic effects, granular temperatures were observed to decrease with increasing air flow rate. This seemed to indicate that fluctuations in particle velocities were caused predominantly by electrostatic forces present within the system. In the absence of electrostatic effects, Figures 17c, d show that granular temperatures were also slightly anisotropic. Although no general relationship between granular temperatures and air flow rate could be discerned, the slightly larger axial components than radial components of granular temperatures in both cases seemed to imply that the flow of air was more important in causing fluctuations in particle velocities during horizontal pneumatic conveying.

Conclusions

Pneumatic transport of granular materials through vertical and horizontal pipes in the presence of electrostatic effects has been investigated computationally using LES and the DEM in this study. The LES numerical results obtained agreed well with the law of the wall for various y^+-ranges. In addition, the maximum value of axial turbulence intensity was observed to be located at around a fixed position irrespective of Reynolds number and therefore the flow behaviors in such systems followed classical scaling. For all cases considered in this study, electrostatic field strength was highest near the pipe walls and degraded toward the pipe center.

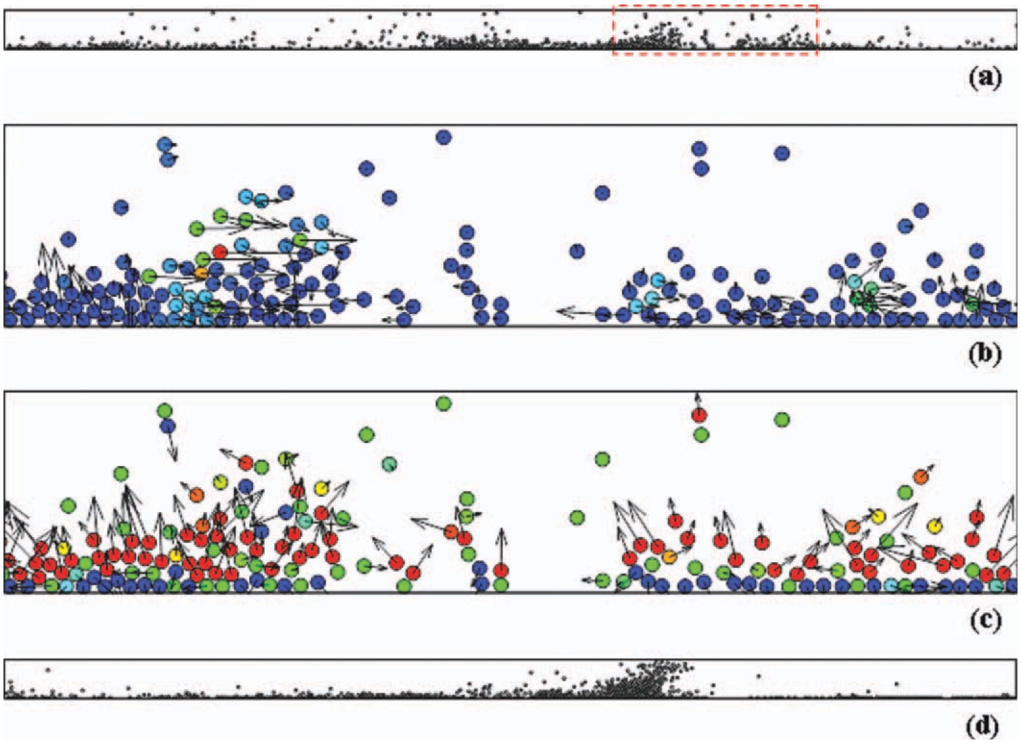

Figure 15. (a) Instantaneous particle distribution during horizontal pneumatic conveying at an air flow rate of 1600 L min^{-1} in the presence of electrostatic effects.

The region marked by a dashed box is enlarged in the next three panels. (b) Instantaneous fluid drag force vectors with color contours indicating magnitudes of axial components of fluid drag forces ranging linearly from 0 N (blue) to 1.0×10^{-4} N (red). (c) Instantaneous interparticle electrostatic repulsion force vectors with color contours indicating radial components of interparticle electrostatic repulsion forces ranging linearly from -10^{-7} N (blue) to 10^{-7} N (red). (d) Instantaneous particle distribution during horizontal pneumatic conveying at an air flow rate of 1600 L min^{-1} in the absence of electrostatic effects. The direction of gravity is downward.

The electrostatic field strength was also seen to increase with decreasing air flow rate. This may be explained by the larger number of particle-wall collisions that occurred and the larger number of particles that remained in contact with the pipe walls at any one instant in time during pneumatic conveying at lower flow rates than at higher flow rates. Typically, through the process of triboelectrification, all particles carry the same type of charges but are charged oppositely to the pipe walls when the state of electrostatic equilibrium has been attained. The DEM simulations showed that a thin layer of particles remained adhered to the pipe walls during the pneumatic conveying process due to the effects of strong

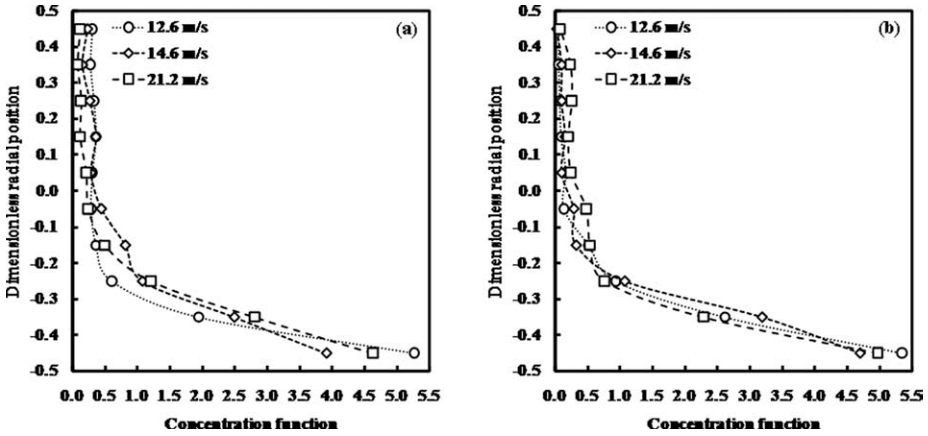

Figure 16. Concentration function profiles during horizontal pneumatic conveying at various average gas velocities in the (a) presence and (b) absence of electrostatic effects.

Radial positions have been nondimensionalized by diameter of pipe.

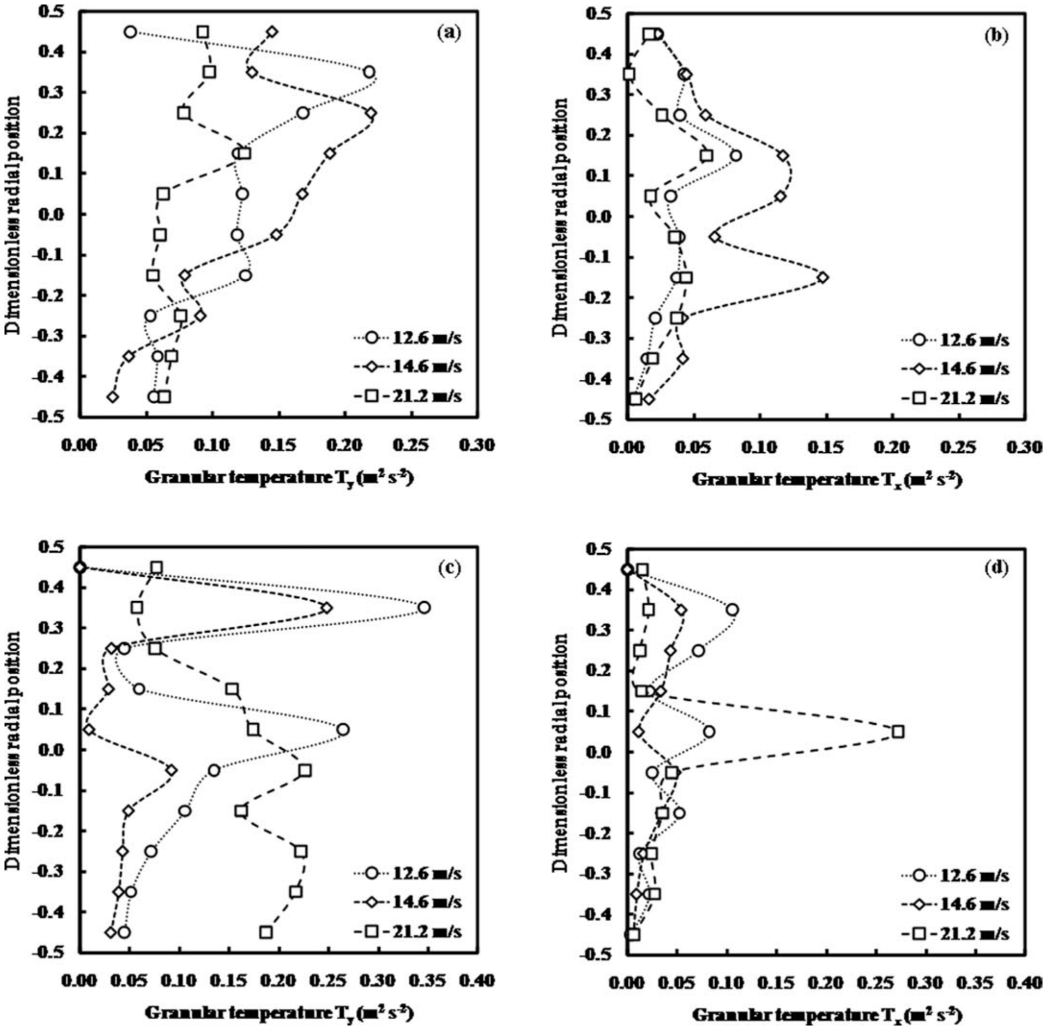

Figure 17. Spatially averaged granular temperature profiles (a) T_y and (b) T_x for horizontal pneumatic conveying in the presence of electrostatic effects as well as (c) T_y and (d) T_x for horizontal pneumatic conveying in the absence of electrostatic effects.

Radial positions have been nondimensionalized by diameter of pipe.

electrostatic forces of attraction towards the pipe walls. Particle concentrations were generally higher near the pipe walls than at the pipe center resulting in the ring flow pattern observed in previous experimental studies. The close correspondence between particle velocity vectors and fluid drag force vectors was indicative of the importance of fluid drag forces in influencing particle behaviors. In contrast, the much weaker particle–particle electrostatic repulsion forces had negligible effects on particle behaviors within the system under all operating conditions considered in this study. Based on dynamic analyses of forces acting on individual particles, it may be concluded that electrostatic effects played a dominant role in influencing particle behaviors during pneumatic conveying through vertical and horizontal pipes at low flow rates, whereas drag forces became more important at high flow rates. It would be pertinent to extend the present study towards investigations of electrostatic effects in pneumatic conveying systems with different operating conditions and material properties. These may include systems operated at different solid loadings or using particles of various sizes, densities or electrostatic charging characteristics. Further, the present numerical strategy can also be applied toward studies of various other types of multiphase or granular systems where electrostatic effects can develop such as circulating fluidized beds, vibrated granular beds, cyclones, and hoppers.

Acknowledgments

This study has been supported by the National University of Singapore under Grant No. R-279-000-275-112. The award of a Lee Kuan Yew Postdoctoral Fellowship to EWCL by the National University of Singapore is gratefully acknowledged.

Literature Cited

1. Yeh SR, Seul M, Shralman BI. Assembly of ordered colloidal aggregates by electric-field-induced fluid flow. *Nature*. 1997;386:57–59.
2. Sapozhnikov MV, Tolmachev YV, Aranson IS, Kwok WK. Dynamic self-assembly and patterns in electrostatically driven granular media. *Phys Rev Lett*. 2003;90:114301.

3. Aranson IS, Blair D, Kalatsky VA, Crabtree GW, Kwok WK, Vinokur VM, Welp U. Electrostatically driven granular media: phase transitions and coarsening. *Phys Rev Lett*. 2000;84:3306–3309.
4. Howell DW, Aronson IS, Crabtree GW. Dynamics of electrostatically driven granular media: effects of humidity. *Phys Rev E*. 2001;63:050301.
5. Yao J, Zhang Y, Wang CH, Matsusaka S, Masuda H. Electrostatics of the granular flow in a pneumatic conveying system. *Ind Eng Chem Res*. 2004;43:7181–7199.
6. Al-Adel MF, Saville DA, Sundaresan S. The effect of static electrification on gas-solid flows in vertical risers. *Ind Eng Chem Res*. 2002;41:6224–6234.
7. Joseph S, Klinzing GE. Vertical gas-solid transition flow with electrostatics. *Powder Technol*. 1983;36:79–87.
8. Smeltzer EE, Weaver ML, Klinzing GE. Individual electrostatic particle interaction in pneumatic transport. *Powder Technol*. 1982;33:31–42.
9. Matsusaka S, Nishida T, Gotoh Y, Masuda H. Electrification of fine particles by impact on a polymer film target. *Adv Powder Technol*. 2003;14:127–138.
10. Yao J, Wang CH. Granular size and shape effect on electrostatics in pneumatic conveying systems. *Chem Eng Sci*. 2006;61:3858–3874.
11. Crowe CT.*Modeling turbulence in multiphase flows*. In:Rodi W,Martelli F, editors. *Engineering Turbulence Modeling and Experiments*, Vol. 2. New York: Elsevier Science, 1993: 899–913.
12. McLaughlin JB. Numerical computation of particle-turbulence interaction. *Int J Multiphase Flow*. 1994;20:211–232.
13. Elghobashi S. On predicting particle-laden turbulent flows. *Appl Sci Res*. 1994;52:309–329.
14. McLaughlin JB. Aerosol particle deposition in numerically simulated channel flow. *Phys Fluids A*. 1989;1:1211–1224.
15. Squires KD, Eaton JK. Measurements of particle dispersion obtained from direct numerical simulations of isotropic turbulence. *J Fluid Mech*. 1991;226:1–35.
16. Elghobashi S, Truesdell GC. Direct simulation of particle dispersion in a decaying isotropic turbulence. *J Fluid Mech*. 1992;242:655–700.
17. Rouson DWI, Eaton JK.*Direct numerical simulation of turbulent channel flow with immersed particles*. In: *Proceedings of the International Symposium on Numerical Methods for Multiphase Flow*. New York: ASME, 1994: 47–57.
18. Elghobashi S, Truesdell GC. On the two-way interaction between homogeneous turbulence and dispersed solid particles. I. Turbulence modification. *Phys Fluids A*. 1993;5:1790–1801.
19. Kim WW, Menon S.*Application of the localized dynamic subgrid-scale model to turbulent wall-bounded flows*. In: *AIAA 35th Aerospace Sciences Meeting*, Vol. 97, Reno, NV, 1997: 210.
20. Lilly DK. A proposed modification of the germano subgrid-scale closure model. *Phys Fluids*. 1992;4:633–635.
21. Unger F, Friedrich R.*Large eddy simulation of fully-developed turbulent pipe flow*. In: *Proceedings of 8th Symposium on Turbulent Shear Flows*, Munich, Germany 1991: 19–3-1–19–3-6.
22. Hager WH. Blasius: a life in research and education. *Exp Fluids*. 2003;34:566–571.
23. Lim EWC. Voidage waves in hydraulic conveying through narrow pipes. *Chem Eng Sci*. 2007;62:4529–4543.
24. Lim EWC. Master curve for the discrete-element method. *Ind Eng Chem Res*. 2008;47:481–485.
25. Lim EWC. Vibrated granular bed on a bumpy surface. *Phys Rev E*. 2009;79:041302.
26. Lim EWC. Density segregation in vibrated granular beds with bumpy surfaces. *AIChE J*. 2010;56:2588–2597.
27. Lim EWC. Granular Leidenfrost effect in vibrated beds with bumpy surfaces. *Eur Phys J E*. 2010;32:365–375.
28. Lim EWC, Wang CH, Yu AB. Discrete element simulation for pneumatic conveying of granular material. *AIChE J*. 2006;52:496–509.
29. Lim EWC, Zhang Y, Wang CH. Effects of an electrostatic field in pneumatic conveying of granular materials through inclined and vertical pipes. *Chem Eng Sci*. 2006;61:7889–7908.
30. Di Felice R. The voidage function for fluid-particle interaction systems. *Int J Multiphase Flow*. 1994;20:153–159.
31. Yao J, Zhang Y, Wang CH, Liang YC. On the electrostatic equilibrium of granular flow in pneumatic conveying systems. *AIChE J*. 2006;52:3775–3793.
32. Prandtl L. Recent results of turbulence research. USA: *NACA TM*720,1933.
33. Kim J, Moin P, Moser R. Turbulence statistics in fully developed channel flow at low Reynolds number. *J Fluid Mech*. 1987;177:133–166.
34. Mochizuki S, Nieuwstadt FTM. Reynolds-number-dependence of the maximum in the streamwise velocity fluctuations in wall turbulence. *Exp Fluids*. 1996;21:218–226.
35. Zagarola MV, Smits AJ. Mean-flow scaling of turbulent pipe flow. *J Fluid Mech*. 1998;373:33–79.
36. Mckeon BJ, Li J, Jiang W, Morrison JF, Smits AJ. Further observations on the mean velocity in fully developed pipe flow. *J Fluid Mech*. 2004;501:135–147.
37. Matida EA, Nishino K, Torii K. Statistical simulation of particle deposition on the wall from turbulent dispersed pipe flow. *Int J Heat Fluid Flow*. 2000;21:389–402.

Manuscript received Dec. 15, 2010, and revision received Feb. 28, 2011.